

One-Vote Veto: Semi-Supervised Learning for Low-Shot Glaucoma Diagnosis

Rui Fan, Christopher Bowd, Nicole Brye, Mark Christopher,
Robert N. Weinreb, David Kriegman, Linda Zangwill
University of California San Diego

{rfan, cbowd, nbrye, mac157, rweinreb, kriegman, lzungwill}@ucsd.edu

Abstract

Convolutional neural networks (CNNs) are a promising technique for automated glaucoma diagnosis from images of the fundus, and these images are routinely acquired as part of an ophthalmic exam. Nevertheless, CNNs typically require a large amount of well-labeled data for training, which may not be available in many biomedical image classification applications, especially when diseases are rare and where labeling by experts is costly.

This paper makes two contributions to address this issue: (1) It extends the conventional twin neural network and introduces a training method for low-shot learning when labeled data are limited and imbalanced, and (2) it introduces a novel semi-supervised learning strategy that uses additional unlabeled training data to achieve greater accuracy. Our proposed multi-task twin neural network (MTTNN) can employ any backbone CNN, and we demonstrate with four backbone CNNs that its accuracy with limited training data approaches the accuracy of backbone CNNs trained with a dataset that is 50 times larger. We also introduce One-Vote Veto (OVV) self-training, a semi-supervised learning strategy that is designed specifically for MTTNNs. By taking both self-predictions and contrastive-predictions of the unlabeled training data into account, OVV self-training provides additional pseudo labels for fine tuning a pre-trained MTTNN. Using a large (imbalanced) dataset with 66715 fundus photographs acquired over 15 years, extensive experimental results demonstrate the effectiveness of low-shot learning with MTTNN and semi-supervised learning with OVV self-training. Three additional, smaller clinical datasets of fundus images acquired under different conditions (cameras, instruments, locations, populations) are used to demonstrate the generalizability of the proposed methods. Source code and pretrained models will be publicly available upon publication.

1. Introduction

Glaucoma is a blinding but treatable disease in which damage to the optic nerve can result in progressive and irreversible vision loss [66]. In 2013, glaucoma affected an estimated 64.3 million individuals worldwide [61]. Because of the rapid global increase in aging populations, 111.8 million cases are expected by 2040 [61]. Improvement in the

management of glaucoma would have a major human and socio-economic impact. Early identification would significantly reduce the economic burden of this disease in its late stages [62]. In addition, studies have shown that visual impairment in glaucoma patients is associated with overall decreases in self-reported vision-related physical activity and mental health [24, 46] as well as an increased risk of involvement in motor vehicle accidents [34, 42].

With recent advances in machine learning, convolutional neural networks (CNNs), trained by supervised learning, have shown their potential to become an effective tool to diagnose glaucoma from fundus images, photographs of the back of eyes [35]. To achieve this, very large amounts of empirical data are required for supervised training. For this work, we use 66715 fundus photographs from the **Ocular Hypertension Treatment Study (OHTS)** [20, 28, 19], a 22-site multi-center, longitudinal (1994-2019) randomized clinical trial of 1636 subjects. The primary goal of the OHTS was to determine if topical ocular hypotensive medications could delay or prevent the onset of glaucoma in eyes with high intraocular pressure [20]. Conversion to glaucoma was decided by a masked endpoint committee of three glaucoma specialists using fundus photographs and visual fields. Owing to its well-characterized ground-truth labels, the OHTS dataset provides us a basis to explore an effective way of training CNNs to diagnose glaucoma with low-shot learning (LSL) when only a small quantity of labeled data is available, and/or semi-supervised learning (SSL) when raw data is abundant, but labeling resources are scarce, costly, require strong expertise, or are just unavailable. We focus specifically on fundus images and glaucoma diagnosis in this paper because we have sufficient data to accurately characterize the effectiveness of our methods. Nonetheless, the same techniques could also be applied to tasks where there is limited data such as rare diseases or where limited labels are available (e.g., asthma and diabetes prediction from fundus images). Therefore, this paper aims to answer the following questions:

1. Can a CNN be developed to accurately diagnose glaucoma, compared to the expert graders of the OHTS? Will the model be generalizable to other datasets?
2. Is it necessary to train CNNs with thousands of labeled fundus images to diagnose glaucoma? Can we use only one image from each patient ($\sim 1.1K$ fundus images in

the OHTS training set)?

3. Can performance be improved further when the CNN trained using a small sample is fine tuned with more unlabeled training data?

To answer these questions, we first evaluate the performance of all state-of-the-art (SOTA) glaucoma diagnosis algorithms (six supervised algorithms [36, 18, 27, 52, 60, 43], one low-shot learning algorithm [31], and two semi-supervised algorithms [3, 15]) on the OHTS [19] dataset. Their generalizabilities are further validated on three additional clinical datasets of fundus images: (a) ACRIMA [16], (b) LAG [35], and (c) DIGS/ADAGES [45].

Moreover, we extend the conventional twin neural network (also known as a Siamese network) to a *multi-task twin neural network (MTTNN)*, as illustrated in Fig. 1. By minimizing a novel *combined weighted cross-entropy loss*, the MTTNN can simultaneously classify a given pair of images and measure their similarity. We explore the feasibility of training a MTTNN to diagnose glaucoma with only 1147 fundus images (one image from each patient). By comparing the results to both fully supervised learning using these 1147 images and to a larger training set of 53K fundus images, we demonstrate that MTTNN greatly reduces overfitting and achieves an accuracy on a small training set comparable to a large training set.

Furthermore, we introduce a novel and effective semi-supervised learning strategy, referred to as One-Vote Veto (OVV) self-training, to generate reliable pseudo labels of the unlabeled training data, which are then incorporated into the labeled training data to fine tune the MTTNNs for better performance and generalizability. Extensive experiments show that the MTTNN fine tuned with OVV self-training performs similarly to the corresponding backbone CNN trained via supervised learning on the OHTS dataset, and achieves higher area under the receiver operating characteristic curve (AUROC) scores on the additional fundus image datasets. The MTTNN fine tuned by OVV self-training performs better than the SOTA semi-supervised glaucoma diagnosis approaches [3, 15], and in some cases, even better than the SOTA supervised approaches.

Two additional few-shot biomedical image classification experiments (see supplement): (a) **chest x-ray image classification** [11, 48], and (b) **lung histopathological image classification** [5], also validate the effectiveness of MTTNN on other types of image data. We believe that our proposed algorithms can be employed to solve a variety of biomedical image classification problems.

In summary, our main contributions include:

- (1) A benchmark of all SOTA glaucoma diagnosis algorithms on the *OHTS dataset*, a newly-released, large-scale, multi-center, longitudinal, extremely-imbalanced clinical dataset of 66715 fundus photographs, acquired under different conditions over 15 years.

- (2) *Multi-task twin neural network*, a novel CNN architecture designed for low/few-shot biomedical image classification. It can be trained easily and efficiently by minimizing a novel loss function. Using such a MTTNN, overfitting can be greatly reduced. It also outperforms the SOTA low-shot glaucoma diagnosis approach [31].

- (3) *One-vote veto self-training*, a new SSL strategy designed to further improve the pretrained MTTNNs. It considers both self-predictions and contrastive-predictions when generating pseudo labels of the unlabeled training data. Extensive experiments on four fundus image datasets valid its effectiveness, where the fine tuned MTTNNs outperform the SOTA semi-supervised glaucoma diagnosis algorithms [3, 15]. Also, they perform similarly, and in some cases, better than the SOTA supervised algorithms.

2. Related Works

Most SOTA glaucoma diagnosis algorithms are developed based on supervised fundus image classification. For example, [27] trains an AlexNet [33] to diagnose glaucoma. Since VGG architectures [53] improved over AlexNet [33] and they can learn more complicated image features, [18] uses a VGG-19 [53] model to learn glaucoma diagnosis. Nevertheless, VGG architectures [53] consist of hundreds of millions of parameters, making them very memory-consuming. By contrast, GoogLeNet [56] and Inception-v3 [57] have lower computational complexities. Hence, [2] and [36] employ transfer learning to retrain an Inception-v3 [57] model (pretrained on the ImageNet [14] database) for glaucoma diagnosis; [52] retrains a pretrained GoogLeNet [56] model to diagnose glaucoma. However, due to vanishing gradients, with the increase of network depth, accuracy gets saturated and then degrades rapidly [21]. To tackle this problem, residual neural network (ResNet) [21] was developed. Due to its robustness, ResNet-50 [21] has been extensively used for biomedical image analysis, and it is a common choice [37, 49, 43, 12, 13] for fundus image classification. Additionally, developing low-cost and real-time embedded glaucoma diagnosis systems [26, 40, 60], *e.g.*, based on MobileNet-v2 [51], for mobile devices is also an emerging area.

Machine/deep learning has achieved compelling performance in data-intensive applications, but it is often difficult for these algorithms to yield comparable performance when only a limited amount of labeled training data is available [65]. Low-shot and semi-supervised learning address these issues. Unfortunately, they are rarely discussed in the glaucoma diagnosis research area. To the best of our knowledge, [31] is the only published low/few-shot glaucoma diagnosis algorithm. It employs a conventional twin neural network to compare two groups of (negative and positive) fundus images. The twin neural network utilizes two identical CNNs to learn visual embeddings. A bidirectional long

short-term memory [67] component is then trained over the CNN outputs for glaucoma diagnosis. However, its training is complicated, as different types of losses are minimized. Also, their achieved glaucoma diagnosis results are unsatisfactory, as each sub-network is only fed with one type (either negative or positive) of fundus images. The lack of same-class comparisons leads to a performance bottleneck, when compared to the MTTNN proposed in this paper.

A thorough search of the relevant literature yielded only two semi-supervised learning algorithms designed specifically for glaucoma diagnosis [15, 3]. [15] uses a deep convolutional generative adversarial network (DCGAN) [47] to learn glaucoma diagnosis in a semi-supervised fashion, where the discriminator simultaneously learns two tasks: (a) classify healthy and glaucomatous optic neuropathy (GON) fundus images, and (b) classify real and fake fundus images. The classifier for the former task is then employed to diagnose glaucoma. [3] is based on self-training [63], a typical SSL approach that requires a pretrained model (typically yielded via supervised learning) to produce pseudo labels of the unlabeled data. However, developing an effective policy to identify reliable predictions to produce pseudo labels is the key to SSL, and the pseudo labels provided by a single pretrained CNN are usually not reliable enough to be used for CNN fine tuning [64]. Moreover, preparing a reliable pretrained classifier with only a small amount of labeled data is notably demanding. In this paper, we combine SSL with LSL to address these issues using glaucoma diagnosis as an example case. Specifically, our proposed OVV self-training strategy, as introduced in Sec. 3.2, is motivated by the mechanism of *learning with external memory*, used in LSL [44], where the labels of unlabeled training data are predicted by a classifier trained via low-shot learning and a small collection of fundus images used to train the classifier.

3. Methodology

3.1. Multi-Task Twin Neural Network

Twin neural networks are commonly utilized for metric learning and few/low-shot image recognition [32]. As its name implies, a twin neural network contains two identical sub-networks. As illustrated in Fig. 1, a given pair of images \mathbf{x}_i and \mathbf{x}_j are separately fed into these sub-networks, which then output two 1D embeddings (features) \mathbf{h}_i and \mathbf{h}_j , respectively. $\Phi(\cdot)$ measures the distance $\mathbf{h}_{i,j}$ between \mathbf{h}_i and \mathbf{h}_j . $\mathbf{h}_{i,j}$ is then followed by a fully connected (FC) layer to produce a scalar $q(\mathbf{x}_i, \mathbf{x}_j) \in [0, 1]$ indicating the similarity between \mathbf{x}_i and \mathbf{x}_j . When \mathbf{x}_i and \mathbf{x}_j are different, $q(\mathbf{x}_i, \mathbf{x}_j)$ approaches 1, and vice versa. $y_i \in \{0, 1\}$ and $y_j \in \{0, 1\}$ denote the ground-truth labels of \mathbf{x}_i and \mathbf{x}_j , respectively, where 0 is healthy and 1 is GON.

However, such a twin neural network can only determine whether \mathbf{x}_i and \mathbf{x}_j belong to the same category instead of

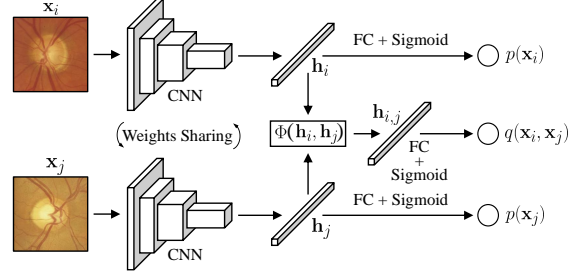


Figure 1: An illustration of our multi-task twin neural network for learning glaucoma diagnosis in a low-shot manner.

predicting their independent categories. A straightforward solution is to separately connect \mathbf{h}_i and \mathbf{h}_j with a FC layer to produce two scalars $p(\mathbf{x}_i)$ and $p(\mathbf{x}_j)$ indicating the probabilities that \mathbf{x}_i and \mathbf{x}_j are GON images, respectively. See Fig. 1 and note that the two FC layers connected to \mathbf{h}_i and \mathbf{h}_j use the same weights. In this paper, we refer to the CNN architecture in Fig. 1 as a MTTNN, which is capable of simultaneously classifying a given pair of fundus images into either healthy or GON as well as measuring their similarity. Using such a task-invariant embedding model, we can have $C(n, 2)$ different combinations of image pairs, where n represents the training sample size. For example, the 1147 fundus images used in the low-shot learning experiments can provide over 657K different image pairs, which can overcome the small sample size issue and reduce overfitting.

In this paper, we use n_0 and n_1 to respectively denote the numbers of healthy and GON fundus images used to train the MTTNN. n_0 is usually much greater than n_1 , because there are fewer patients with glaucomatous disease than healthy patients, resulting in a severely imbalanced dataset. In this regard, we apply two weights $\omega_{\text{cla}} = \frac{n_0}{n_0 + n_1}$ and $\omega_{\text{sim}} = \frac{n_0(n_0 - 1) + n_1(n_1 - 1)}{(n_0 + n_1)(n_0 + n_1 - 1)}$ to weigh the fundus image classification loss \mathcal{L}_{cla} and the input similarity measurement loss \mathcal{L}_{sim} , respectively. ω_{cla} denotes the proportion of healthy fundus images in the training set, while ω_{sim} represents the proportion of the cases that the given labeled fundus image pairs $\mathbf{z} = [(\mathbf{x}_i, y_i), (\mathbf{x}_j, y_j)]$ belong to the same category. We train the MTTNN by minimizing a combined weighted cross-entropy loss, as follows:

$$\mathcal{L}(\mathbf{z}) = \lambda \mathcal{L}_{\text{cla}}(\mathbf{z}) + \mathcal{L}_{\text{sim}}(\mathbf{z}), \quad (1)$$

where

$$\begin{aligned} \mathcal{L}_{\text{cla}}(\mathbf{z}) = & - \left(\omega_{\text{cla}} (y_i \log(p(\mathbf{x}_i)) + y_j \log(p(\mathbf{x}_j))) \right. \\ & + (1 - \omega_{\text{cla}}) ((1 - y_i) \log(1 - p(\mathbf{x}_i)) \\ & \left. + (1 - y_j) \log(1 - p(\mathbf{x}_j))) \right), \end{aligned} \quad (2)$$

$$\begin{aligned} \mathcal{L}_{\text{sim}}(\mathbf{z}) = & - \left(\omega_{\text{sim}} |y_i - y_j| \log(q(\mathbf{x}_i, \mathbf{x}_j)) \right. \\ & \left. + (1 - \omega_{\text{sim}}) (1 - |y_i - y_j|) \log(1 - q(\mathbf{x}_i, \mathbf{x}_j)) \right), \end{aligned} \quad (3)$$

λ is a hyper-parameter used to balance \mathcal{L}_{cla} and \mathcal{L}_{sim} . The selection of λ and $\Phi(\cdot)$ is discussed in the supplement. The motivations of using such a combined weighted cross-entropy loss function instead of the commonly used triplet loss [22] or contrastive loss [30] to train the MTTNN are:

1. Most datasets for rare disease diagnosis are imbalanced. As detailed in Sec. 4.1, the OHTS training set is severely imbalanced (50208 healthy images vs. 2416 GON images for supervised learning; 995 healthy images vs. 152 GON images for low-shot learning). Learning from such an imbalanced dataset without weights on different classes can result in many incorrect predictions (most GON images are likely to be predicted as healthy images). In this regard, a higher weight should be used for the minority class so as to prevent CNN from predicting all the images as the majority class.
2. It is usually difficult to weigh different types of losses, e.g., regression and classification, in multi-task learning [29]. An undesirable weight can result in a poorly-performing task when other tasks converge to satisfactory results. Therefore, formulating \mathcal{L}_{sim} as a weighted cross-entropy loss function is a simple but effective solution. However, due to the dataset imbalance problem discussed above, ω_{sim} is included in (16).
3. As shown in Fig. 2, OVV self-training requires both labels and probabilities (of being GON images), predicted by a pretrained model, to produce pseudo labels of the unlabeled data. Such network architecture and training loss can efficiently and effectively provide both “self-predicted” and “contrastively-predicted” labels and probabilities, as explained in Sec. 3.2.

It should be noted here that the images from the same patient are not used as an image pair for MTTNN training. The comparisons between LSL and fully supervised learning on a small training set are given in the supplement.

3.2. One-Vote Veto Self-Training

As introduced in Sec. 2, self-training aims to improve the performance of a pretrained model by incorporating reliable predictions of the unlabeled data to obtain useful additional information that can be used for model fine tuning. A feasible strategy to determine such reliable predictions is, therefore, the key to self-training [41].

For conventional SSL algorithms, given a pretrained image classification model (through supervised learning), a straightforward way to determine whether an unlabeled image is reliable enough to be included for model fine tuning is to compare its probability distributed to the most possible class, with a predetermined threshold. If its probability exceeds that threshold, its prediction will be considered as a pseudo label. The image and its pseudo label will then be used to fine tune the pretrained model.

Algorithm 1: One-Vote Veto self-training strategy.

Data: $\mathcal{X}^r, \mathcal{Y}^r$, and \mathcal{X}^t

```

1 while Training do
2   Given a mini-batch consisting of
      $\{\mathbf{x}_1^r, \dots, \mathbf{x}_m^r\} \in \mathcal{X}^r$ ,  $\{y_1^r, \dots, y_m^r\} \in \mathcal{Y}^r$  and
      $\{\mathbf{x}_1^t, \dots, \mathbf{x}_m^t\} \in \mathcal{X}^t$ ;
      $\mathcal{P} \leftarrow \emptyset$ ;
3   for  $i \leftarrow 1$  to  $m$  do
4     if  $(|p(\mathbf{x}_i^t) - \frac{1}{2}| > \frac{1}{2} - \kappa_2)$  then
5        $w \leftarrow 0$ ;
6       for  $j \leftarrow 1$  to  $m$  do
7         if  $|p(\mathbf{x}_j^r) - y_j^r| < \kappa_2$ 
8           then
9              $w \leftarrow w + 1$ ;
10             $\mathcal{P} \leftarrow \mathcal{P} \cup \{\mathbf{x}_j^r, y_j^r\}$ ;
11             $\mathbf{v}_1(j) \leftarrow \tilde{y}_i^{r \rightarrow t}(\mathbf{x}_j^r, \mathbf{x}_i^t)$ ;
12             $\mathbf{v}_2(j) \leftarrow p^{r \rightarrow t}(\mathbf{x}_j^r, \mathbf{x}_i^t)$ ;
13          if  $(\sum_{j=1}^m \mathbf{v}_1(j) \leq \kappa_1 \vee \sum_{j=1}^m \mathbf{v}_2(j) \geq w - \kappa_1)$ 
14            and  $\text{any } |\mathbf{v}_2(j) - \frac{1}{2}| > \frac{1}{2} - \kappa_2$ 
15              then
16                 $\mathcal{P} \leftarrow \mathcal{P} \cup \{\mathbf{x}_i^t, \tilde{y}_i^t\}$ 
17   fine tune the target model using unique( $\mathcal{P}$ );
18 if the target model outperforms the reference model then
19   Update the reference model parameters;
```

However, relying on probability distributions alone to generate pseudo labels is not often sufficient [63]. Inspired by learning with external memory [55], we introduce *One-Vote Veto self-training* in this paper, as illustrated in Fig. 2. Similar to learning with external memory [55], we use a collection of m reference (labeled) fundus images $\{\mathbf{x}_1^r, \dots, \mathbf{x}_m^r\} \in \mathcal{X}^r$ to provide “contrastive predictions” to the target (unlabeled) fundus images $\{\mathbf{x}_1^t, \dots, \mathbf{x}_m^t\} \in \mathcal{X}^t$, where the superscripts r and t denote “reference” and “target”, respectively. The contrastive predictions then vote to veto the unreliable “self-predictions” $\{\tilde{y}_1^t, \dots, \tilde{y}_m^t\}$ produced by the MTTNN. Our OVV self-training is detailed in Algorithm 1, where the target model updates its parameters during self-training but the reference model does not.

When fine tuning a MTTNN pretrained through LSL, each mini-batch contains a discrete set of m reference fundus images $\{\mathbf{x}_1^r, \dots, \mathbf{x}_m^r\} \in \mathcal{X}^r$, their ground-truth labels $\{y_1^r, \dots, y_m^r\} \in \mathcal{Y}^r$, and the same number of m target fundus images $\{\mathbf{x}_1^t, \dots, \mathbf{x}_m^t\} \in \mathcal{X}^t$ without labels. \mathbf{h}_k^r and \mathbf{h}_k^t represent the 1D embeddings learned from \mathbf{x}_k^r and \mathbf{x}_k^t ($k \in [1, m] \cap \mathbb{Z}$), respectively. Given a pair of reference and target fundus images, \mathbf{x}_q^r and \mathbf{x}_k^t , the pretrained MTTNN can “self-predict”: (a) the scalars $p(\mathbf{x}_q^r)$ and $p(\mathbf{x}_k^t)$ which indicate the probabilities that \mathbf{x}_q^r and \mathbf{x}_k^t are GON images, respectively, and (b) their labels $\tilde{y}_q^r = \delta(p(\mathbf{x}_q^r))$ and $\tilde{y}_k^t = \delta(p(\mathbf{x}_k^t))$ using its fundus image classification functionality ($\delta(p) = 1$ when $p > 0.5$, and $\delta(p) = 0$ otherwise). $p(\mathbf{x}_q^r)$ is then used to determine whether the refer-

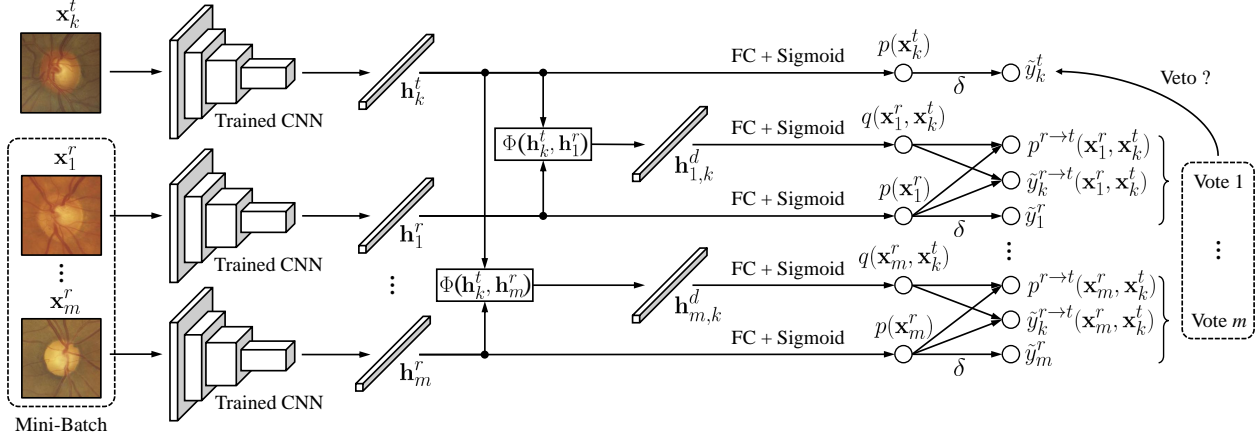


Figure 2: An illustration of our *One-Vote Veto self-training* strategy. $\mathbf{h}_{1,k}^d$ and $\mathbf{h}_{m,k}^d$ are two 1D embeddings, followed by a FC layer to produce scalars indicating the similarities between the given pairs of reference and target fundus images.

ence fundus image \mathbf{x}_q^r is qualified to veto unreliable predictions. If $|p(\mathbf{x}_q^r) - y_q^r| > \kappa_2$, we will omit its vote, where κ_2 is a threshold used to select qualified reference fundus images. In the meantime, the pretrained MTTNN can also “contrastively-predict” the scalar

$$p^{r \rightarrow t}(\mathbf{x}_q^r, \mathbf{x}_k^t) = |p(\mathbf{x}_q^r) - q(\mathbf{x}_q^r, \mathbf{x}_k^t)| \quad (4)$$

indicating the GON probability as well as the label

$$\tilde{y}_k^{r \rightarrow t}(\mathbf{x}_q^r, \mathbf{x}_k^t) = |\delta(p(\mathbf{x}_q^r)) - \delta(q(\mathbf{x}_q^r, \mathbf{x}_k^t))| \quad (5)$$

of \mathbf{x}_k^t from \mathbf{x}_q^r using its input similarity measurement functionality. Please note: in many cases, $\tilde{y}_k^{r \rightarrow t}(\mathbf{x}_q^r, \mathbf{x}_k^t)$ is unequal to $\delta(p^{r \rightarrow t}(\mathbf{x}_q^r, \mathbf{x}_k^t))$. In order to determine whether \tilde{y}_k^t is reliable and can be used as the pseudo label of \mathbf{x}_k^t , all the reference fundus images $\{\mathbf{x}_1^r, \dots, \mathbf{x}_m^r\} \in \mathcal{X}^r$ in the mini-batch are used to provide additional judgements. Each pair of contrastively-predicted scalar (indicating GON probability) and label form a vote ($p^{r \rightarrow t}(\mathbf{x}_q^r, \mathbf{x}_k^t), \tilde{y}_k^{r \rightarrow t}(\mathbf{x}_q^r, \mathbf{x}_k^t)$). With all votes collected from the qualified reference fundus images, the OVV self-training algorithm determines whether \tilde{y}_k^t should be used as the pseudo label for \mathbf{x}_k^t based on the following criteria:

- Identical to the manner of determining qualified reference fundus images, if any $p^{r \rightarrow t}(\mathbf{x}_j^r, \mathbf{x}_k^t)$ ($j \in [1, m] \cap \mathbb{Z}$) or $p(\mathbf{x}_k^t)$ is not close to either 0 (healthy) or 1 (GON), evaluated by the threshold κ_2 , \tilde{y}_k^t will not be assigned to \mathbf{x}_k^t .
- If a minority of more than κ_1 qualified reference fundus images disagree with the majority of the qualified reference fundus images, \tilde{y}_k^t will not be assigned to \mathbf{x}_k^t .

As discussed in Sec. 4, $\kappa_1 = 0$ (all the qualified reference images vote to the same category) achieves the best overall performance. In this regard, the above-mentioned strategy is named “*One-Vote Veto*” in this paper. Since each target fundus image is required to be compared with all the

reference fundus images in the same mini-batch, the proposed self-training strategy has a computational complexity of $\mathcal{O}(n^2)$, which is relatively memory-consuming. The reliable target fundus images and their pseudo labels are then included into the low-shot training data to fine tune the pretrained MTTNN with supervised learning by minimizing a weighted cross-entropy loss. The OVV self-training performance with respect to different κ_1 , κ_2 and m is discussed in Sec. 4.

4. Experiments

4.1. Datasets and Experimental Setups

The datasets utilized in our experiments were collected at various intervals by different clinicians from different institutes using different fundus cameras. The ACRIMA [16] and LAG [35] datasets are publicly available, while the OHTS [20, 28] and DIGS/ADAGES [45] datasets are available upon request after appropriate data use agreements are initiated. Their details follow:

- **OHTS:** The OHTS is the only **multi-center longitudinal study** that has precise information on the dates/timing of the development of glaucoma (the enrolled subjects did not have glaucoma at study entry) using standardized assessment criteria by an independent Optic Disc Reading Center and confirmed by three glaucoma specialist endpoint committee members. In our experiments, a square region centered on the optic nerve head was first extracted from each raw fundus image using a well-trained DeepLabv3+ [9] model. A small part of the raw data are stereoscopic fundus images, each of which was split to produce two individual fundus images. This image pre-processing resulted in a total number of 74768 fundus images. Moreover, ENPOAGDISC (endpoint committee attributable to primary open angle glaucoma based on optic disc changes from photographs) labels are used as

the classification ground truth. The total number of fundus images are divided into a training set (50208 healthy images and 2416 GON images), a validation set (7188 healthy images and 426 GON images), and a test set (13780 healthy images and 660 GON images) by participant. Please note: all images from each patient are in only one of these three subsets. Additionally, we select one image from each patient in the training set to create the low-shot training set (995 healthy images and 152 GON images).

- **ACRIMA:** The ACRIMA [16] dataset consists of 309 healthy images and 396 GON images. It was collected as part of an initiative by the government of Spain. Classification was based on the review by a single experienced glaucoma expert. Images were excluded if they did not provide a clear view of the optic nerve head region [13].
- **LAG:** The LAG [35] dataset contains 3143 healthy images and 1711 GON images¹, obtained from Beijing Tongren Hospital. Similar to the OHTS dataset, we also use the well-trained DeepLabv3+ [9] model to extract a square region centered on the optic nerve head from each fundus image.
- **DIGS/ADAGES:** The UCSD-based Diagnostic Innovations in Glaucoma Study (DIGS) and African Descent and Glaucoma Evaluation Study (ADAGES) [45] are longitudinal studies designed to detect and monitor glaucoma based on optical imaging and visual function testing that, when combined, have generated tens of thousands of test results from over 4000 healthy, glaucoma suspect or glaucoma eyes. In our experiments, we utilize the DIGS/ADAGES test set (5184 healthy images and 4289 GON images) to evaluate the generalizability of our proposed methods.

Visualizations of the four test sets using t-SNE [39] are provided in the supplement. Since healthy and GON images are distributed similarly between the OHTS and LAG datasets, we expect models to perform similarly on these datasets. Dissimilar distributions in the ACRIMA and DIGS/ADAGES datasets led us to believe the performance of models on these datasets would be somewhat worse. Using these four datasets, we conduct three experiments:

1. **Supervised learning experiment:** We employ transfer learning [58] to train ResNet-50 [21], MobileNet-v2 [51], DenseNet [23] and EfficientNet [59] (pretrained on the ImageNet database [14]), on the **entire OHTS training set (including 53K images)**. The best-performing models are selected using the OHTS validation set. Their performances are subsequently evaluated on the OHTS test set, the ACRIMA dataset, the LAG dataset, and the DIGS/ADAGES test set.
2. **Low-shot learning experiment:** The four models mentioned above (pretrained on the ImageNet database [14]) are used as MTTNN backbones and trained on the OHTS low-shot training set (1147 images) to validate performance for low-shot glaucoma diagnosis. The validation and testing procedures are identical to those in the supervised learning experiment.
3. **Semi-supervised learning experiment:** The well-trained MTTNNs are fine tuned on the entire OHTS training set without using any ground-truth labels. The fine tuned MTTNNs are referred to as **MTTNN+OVV**. The validation and testing procedures are identical to those in the supervised learning experiment.

The fundus images are resized to 224×224 pixels. The initial learning rate is set to 0.001, which decays gradually after the 100th epochs. Due to the dataset imbalance problem, F-score (Fsc) is utilized to select the best-performing models during the validation stage. Moreover, we adopt an early stopping mechanism during the validation stage to reduce overfitting, namely, the training will be terminated if the achieved Fsc has not increased for 30 epochs. In addition, we use three metrics: 1) accuracy (ACC), 2) Fsc, and 3) AUROC to quantify the performances of the trained models. Additional performance evaluation with more details is provided in the supplement.

4.2. Performance comparison of supervised learning, LSL, and SSL for glaucoma diagnosis

Comparisons of supervised learning, low-shot learning, and semi-supervised learning (w.r.t. four backbone CNNs: ResNet-50 [21], MobileNet-v2 [51], DenseNet [23], and EfficientNet [59]) for glaucoma diagnosis are provided in Tab. 1. First, these results suggest that the MTTNNs fine tuned with OVV self-training that requires a small number of labeled images perform similarly (AUROC 95% CI overlaps considerably) and, in some cases, significantly better (AUROC 95% CI does not overlap) than the backbone CNNs trained with a large number of labeled images (50 times larger) under full supervision.

Specifically, when using ResNet-50 [21], MobileNet-v2 [51], or DenseNet [23] as the backbone CNN, SSL performs similarly to supervised learning on the OHTS and DIGS/ADAGES test sets, and in most cases significantly better than supervised learning on the ACRIMA and LAG datasets. Although EfficientNet [59] trained through supervised learning performs unsatisfactorily on all four test sets, it shows considerable compatibility with MTTNN in the LSL and SSL experiments. Second as expected, the AUROC scores achieved by LSL are in most, but not all, cases slightly lower than those achieved by the backbone CNNs, when evaluated on the OHTS test set. However, LSL shows better generalizability than supervised learning on the ACRIMA and LAG datasets. Moreover, since LSL

¹The number of fundus images being published is fewer than what was reported in publication [35].

Backbone	Method	Training strategy	OHTS [19]	ACRIMA [16]	LAG [35]	DIGS/ADAGES [45]	t (min)
ResNet-50 [21]	Baseline	Supervised learning	0.904 (95% CI: 0.865, 0.935)	0.736 (95% CI: 0.698, 0.771)	0.794 (95% CI: 0.780, 0.807)	0.744 (95% CI: 0.696, 0.792)	52.1
	MTTNN	Low-shot learning	0.869 (95% CI: 0.833, 0.901)	0.758 (95% CI: 0.723, 0.792)	0.841 (95% CI: 0.829, 0.853)	0.743 (95% CI: 0.683, 0.795)	1.8
	MTTNN+OVV	Semi-supervised learning	0.898 (95% CI: 0.857, 0.928)	0.775 (95% CI: 0.741, 0.808)	0.881 (95% CI: 0.870, 0.891)	0.763 (95% CI: 0.695, 0.820)	203.7
MobileNet-v2 [51]	Baseline	Supervised learning	0.893 (95% CI: 0.845, 0.932)	0.794 (95% CI: 0.760, 0.825)	0.856 (95% CI: 0.844, 0.867)	0.786 (95% CI: 0.728, 0.835)	42.9
	MTTNN	Low-shot learning	0.859 (95% CI: 0.813, 0.896)	0.820 (95% CI: 0.786, 0.850)	0.843 (95% CI: 0.831, 0.855)	0.748 (95% CI: 0.689, 0.802)	1.2
	MTTNN+OVV	Semi-supervised learning	0.887 (95% CI: 0.850, 0.920)	0.840 (95% CI: 0.808, 0.867)	0.851 (95% CI: 0.838, 0.862)	0.777 (95% CI: 0.718, 0.826)	125.4
DenseNet [23]	Baseline	Supervised learning	0.898 (95% CI: 0.867, 0.927)	0.810 (95% CI: 0.778, 0.841)	0.784 (95% CI: 0.771, 0.798)	0.743 (95% CI: 0.688, 0.789)	122.7
	MTTNN	Low-shot learning	0.854 (95% CI: 0.811, 0.894)	0.753 (95% CI: 0.716, 0.786)	0.853 (95% CI: 0.842, 0.865)	0.732 (95% CI: 0.675, 0.785)	5.7
	MTTNN+OVV	Semi-supervised learning	0.896 (95% CI: 0.861, 0.926)	0.783 (95% CI: 0.748, 0.817)	0.831 (95% CI: 0.818, 0.843)	0.746 (95% CI: 0.678, 0.800)	324.0
EfficientNet [59]	Baseline	Supervised learning	0.768 (95% CI: 0.684, 0.834)	0.633 (95% CI: 0.590, 0.672)	0.650 (95% CI: 0.634, 0.667)	0.658 (95% CI: 0.611, 0.702)	48.7
	MTTNN	Low-shot learning	0.863 (95% CI: 0.818, 0.899)	0.845 (95% CI: 0.815, 0.873)	0.845 (95% CI: 0.833, 0.856)	0.719 (95% CI: 0.659, 0.774)	1.5
	MTTNN+OVV	Semi-supervised learning	0.886 (95% CI: 0.845, 0.918)	0.792 (95% CI: 0.758, 0.824)	0.850 (95% CI: 0.837, 0.861)	0.749 (95% CI: 0.690, 0.800)	159.8

Table 1: AUROC (shown along with 95% CI) and training time per epoch t (min) of supervised learning, low-shot learning and semi-supervised learning for glaucoma diagnosis.

Percentage (%) of Training Data	MTTNN			MTTNN + OVV		
	ACC (%)	Fsc (%)	AUROC	ACC (%)	Fsc (%)	AUROC
0.5	84.769	20.228	0.759	88.856	25.351	0.797
1.0	88.538	25.654	0.806	88.453	32.472	0.857
2.0 (baseline)	87.150	31.726	0.865	91.415	41.148	0.898
10.0	89.988	38.612	0.891	91.446	39.760	0.899
50.0	94.223	40.826	0.887	92.067	38.187	0.889
90.0	92.897	41.878	0.887	93.331	43.421	0.898

(a) Backbone CNN: ResNet-50 [21]

Percentage (%) of Training Data	MTTNN			MTTNN + OVV		
	ACC (%)	Fsc (%)	AUROC	ACC (%)	Fsc (%)	AUROC
0.5	81.954	18.035	0.745	87.918	29.246	0.826
1.0	91.764	20.628	0.772	89.407	31.357	0.841
2.0 (baseline)	86.018	30.252	0.854	90.609	36.960	0.887
10.0	89.562	36.808	0.897	89.624	36.887	0.888
50.0	91.043	39.050	0.888	93.230	40.653	0.889
90.0	93.750	37.519	0.890	91.857	41.602	0.896

(b) Backbone CNN: MobileNet-v2 [51]

Table 2: Comparisons w.r.t. different percentages of labeled training data. The baseline experiments utilize 1147 labeled fundus images ($\sim 2\%$ of full training set).

uses only a small amount of training data, training a MTTNN is much faster than supervised learning. As MTTNNs assembled with ResNet-50 [21] and MobileNet-v2 [51] typically demonstrate better performances than the ones assembled with DenseNet [23] and EfficientNet [59], we only use the former two CNNs for the following experiments.

We also carry out a series of experiments w.r.t. different percentages of training data, as shown in Tab. 2, to further validate the effectiveness of our proposed LSL and SSL algorithms. When using less labeled training data (0.5% and 1.0%), the MTTNN performance degrades. However, its performance can still be greatly improved with OVV self-training (ACC, Fsc, and AUROC can be improved by up to 6%, 11%, and 0.08, respectively). In addition, when using over 10% of the entire training data, the MTTNN performance saturates, and the OVV self-training can bring very limited improvements on MTTNNs.

4.3. Ablation study

Furthermore, we discuss the selection of the thresholds κ_1 and κ_2 (used to select reliable “self-predictions” and “contrastive-predictions” in our OVV self-training) as well as the impact of different mini-batch sizes $2m$ on OVV self-training (each mini-batch contains m pairs of reference and

Dataset	κ_1	κ_2	m	ACC (%)	Fsc (%)	AUROC
OHTS [20, 28]	0	0.01	20	91.415 \uparrow	41.148 \uparrow	0.898 \uparrow
	0	0.01	15	92.113 \uparrow	41.316 \uparrow	0.898 \uparrow
	0	0.01	10	94.199 \uparrow	43.759 \uparrow	0.890 \uparrow
	0	0.1	20	90.516 \uparrow	38.139 \uparrow	0.898 \uparrow
	2	0.01	20	90.717 \uparrow	35.818 \uparrow	0.885 \uparrow
	2	0.1	20	92.656 \uparrow	32.017 \uparrow	0.851 \downarrow
	4	0.01	20	92.610 \uparrow	29.668 \downarrow	0.854 \downarrow
	4	0.1	20	92.672 \uparrow	28.463 \downarrow	0.842 \downarrow
	0	0.01	20	59.858 \downarrow	49.192 \downarrow	0.775 \uparrow
	0	0.01	15	60.426 \downarrow	49.365 \downarrow	0.751 \downarrow
ACRIMA [16]	0	0.01	10	54.610 \downarrow	35.743 \downarrow	0.721 \downarrow
	0	0.01	20	80.882 \uparrow	66.304 \uparrow	0.881 \uparrow
	0	0.01	15	76.864 \downarrow	56.252 \downarrow	0.825 \uparrow
LAG [35]	0	0.01	10	76.638 \downarrow	56.518 \downarrow	0.826 \downarrow
	0	0.01	20	67.813 \uparrow	58.315 \uparrow	0.763 \uparrow
	0	0.01	15	63.045 \downarrow	44.727 \downarrow	0.753 \downarrow
DIGS/ADAGES [45]	0	0.01	10	61.819 \downarrow	41.340 \downarrow	0.727 \downarrow

(a) Backbone CNN: ResNet-50 [21]

Dataset	κ_1	κ_2	m	ACC (%)	Fsc (%)	AUROC
OHTS [20, 28]	0	0.01	25	90.609 \uparrow	36.960 \uparrow	0.887 \uparrow
	0	0.01	20	93.470 \uparrow	36.976 \uparrow	0.893 \uparrow
	0	0.01	15	93.742 \uparrow	37.779 \uparrow	0.863 \uparrow
	0	0.1	25	88.825 \uparrow	34.351 \uparrow	0.878 \uparrow
	2	0.01	25	93.463 \uparrow	35.204 \uparrow	0.862 \uparrow
	2	0.1	25	90.772 \uparrow	32.616 \uparrow	0.858 \uparrow
	4	0.01	25	92.268 \uparrow	31.852 \uparrow	0.854 \uparrow
	4	0.1	25	90.803 \uparrow	32.690 \uparrow	0.859 \uparrow
	0	0.01	25	72.340 \uparrow	70.229 \uparrow	0.840 \uparrow
	0	0.01	20	63.404 \downarrow	54.895 \downarrow	0.814 \downarrow
ACRIMA [16]	0	0.01	15	61.986 \downarrow	51.273 \downarrow	0.826 \uparrow
	0	0.01	25	79.625 \uparrow	65.262 \downarrow	0.851 \uparrow
	0	0.01	20	76.670 \downarrow	55.906 \downarrow	0.841 \downarrow
LAG [35]	0	0.01	15	75.834 \downarrow	51.748 \downarrow	0.866 \uparrow
	0	0.01	25	69.653 \uparrow	63.258 \downarrow	0.777 \uparrow
	0	0.01	20	66.383 \downarrow	52.888 \downarrow	0.773 \uparrow
DIGS/ADAGES [45]	0	0.01	15	63.965 \downarrow	44.198 \downarrow	0.789 \uparrow

(b) Backbone CNN: MobileNet-v2 [51]

Table 3: Evaluation of our OVV self-training w.r.t. different κ_1 , κ_2 and m . The best results are shown in bold font. \uparrow indicates SSL outperforms LSL.

target fundus images). Tab. 3 shows the MTTNN performances with respect to different κ_1 , κ_2 and m . When evaluated on the OHTS test set, it can be seen that ACC and Fsc increase slightly but AUROC almost remain the same, with the decrease of m . Moreover, with the increase of κ_1 and κ_2 , the standard to determine reliable predictions becomes lower, making the SSL performance degrade. Based on this experiment, we believe OVV self-training benefits from smaller κ_1 and κ_2 .

Additionally, MTTNNs, trained under different m , are also evaluated on the three additional test sets, as shown in Tab. 3. It can be seen that the network trained under a larger m typically shows better results. When m decreases,

Training strategy	Method	ACC (%)	Fsc (%)	AUROC
Supervised learning	Li <i>et al.</i> [36]	93.812	42.590	0.886
	Gómez-Valverde <i>et al.</i> [18]	95.068	48.039	0.903
	Judy <i>et al.</i> [27]	94.188	42.835	0.908
	Serener and Serte [52]	90.492	41.227	0.912
	Thakur <i>et al.</i> [60]	94.145	44.115	0.896
	Medeiros <i>et al.</i> [43]	93.261	43.016	0.904
Low-shot learning	Kim <i>et al.</i> [31]	84.203	23.161	0.786
	* MTTNN (ResNet-50)	87.150	31.726	0.865
	* MTTNN (MobileNet-v2)	86.018	30.252	0.854
Semi-supervised learning	Al Ghamdi <i>et al.</i> [3]	84.808	27.579	0.830
	Diaz-Pinto <i>et al.</i> [15]	76.619	20.721	0.748
	* MTTNN (ResNet-50) + OVV	90.244	38.454	0.899
	* MTTNN (MobileNet-v2) + OVV	89.360	36.599	0.891

(a) OHTS [28] test set.

Training strategy	Method	ACC (%)	Fsc (%)	AUROC
Supervised learning	Li <i>et al.</i> [36]	60.142	46.272	0.813
	Gómez-Valverde <i>et al.</i> [18]	63.546	53.358	0.826
	Judy <i>et al.</i> [27]	57.872	41.650	0.824
	Serener and Serte [52]	54.326	36.364	0.675
	Thakur <i>et al.</i> [60]	65.106	58.020	0.794
	Medeiros <i>et al.</i> [43]	53.333	31.601	0.736
Low-shot learning	Kim <i>et al.</i> [31]	64.965	58.627	0.844
	* MTTNN (ResNet-50)	67.092	63.175	0.758
	* MTTNN (MobileNet-v2)	70.355	67.797	0.820
Semi-supervised learning	Al Ghamdi <i>et al.</i> [3]	68.511	67.257	0.794
	Diaz-Pinto <i>et al.</i> [15]	59.149	44.828	0.818
	* MTTNN (ResNet-50) + OVV	64.539	57.627	0.801
	* MTTNN (MobileNet-v2) + OVV	72.340	70.939	0.835

(b) ACRIMA [16] dataset.

Training strategy	Method	ACC (%)	Fsc (%)	AUROC
Supervised learning	Li <i>et al.</i> [36]	76.535	53.756	0.855
	Gómez-Valverde <i>et al.</i> [18]	80.202	62.417	0.883
	Judy <i>et al.</i> [27]	78.348	60.174	0.860
	Serener and Serte [52]	77.379	66.545	0.806
	Thakur <i>et al.</i> [60]	80.305	65.882	0.856
	Medeiros <i>et al.</i> [43]	75.052	50.267	0.794
Low-shot learning	Kim <i>et al.</i> [31]	74.619	65.000	0.805
	* MTTNN (ResNet-50)	79.028	65.908	0.841
	* MTTNN (MobileNet-v2)	79.007	69.482	0.843
Semi-supervised learning	Al Ghamdi <i>et al.</i> [3]	79.028	72.382	0.860
	Diaz-Pinto <i>et al.</i> [15]	65.554	56.662	0.701
	* MTTNN (ResNet-50) + OVV	81.644	69.929	0.879
	* MTTNN (MobileNet-v2) + OVV	80.470	68.692	0.849

(c) LAG [35] dataset.

Training strategy	Method	ACC (%)	Fsc (%)	AUROC
Supervised learning	Li <i>et al.</i> [36]	65.293	46.955	0.780
	Gómez-Valverde <i>et al.</i> [18]	65.157	45.729	0.795
	Judy <i>et al.</i> [27]	63.556	41.144	0.760
	Serener and Serte [52]	69.108	57.478	0.757
	Thakur <i>et al.</i> [60]	70.606	60.322	0.786
	Medeiros <i>et al.</i> [43]	62.500	38.042	0.744
Low-shot learning	Kim <i>et al.</i> [31]	63.862	52.949	0.687
	* MTTNN (ResNet-50)	67.745	60.754	0.743
	* MTTNN (MobileNet-v2)	69.176	68.145	0.748
Semi-supervised learning	Al Ghamdi <i>et al.</i> [3]	64.850	54.816	0.716
	Diaz-Pinto <i>et al.</i> [15]	64.441	59.908	0.677
	* MTTNN (ResNet-50) + OVV	66.281	55.486	0.747
	* MTTNN (MobileNet-v2) + OVV	70.402	66.015	0.776

(d) DIGS/ADAGES [45] test set.

Table 4: Comparisons with other SOTA glaucoma diagnosis algorithms. * denotes our methods. The best results of each training strategy are shown in bold font.

the generalizability of MTTNN degrades dramatically, especially for Fsc (decreases by around 9-19%). Therefore, increasing the mini-batch size can improve the MTTNN generalizability, as more reference fundus images are used to provide contrastive-predictions for the target fundus images, which can veto more unreliable predictions on the unlabeled data. Hence, we increase m to 30 to further improve OVV self-training when comparing it with other published SOTA algorithms, as shown in Sec. 4.4. Since our threshold

selection experiments cover a very limited number of discrete sets of κ_1 , κ_2 , and m , we believe better performance can be achieved when more values are tested.

4.4. Comparisons with other SOTA glaucoma diagnosis approaches

Tab. 4 provides comprehensive comparisons with nine SOTA glaucoma diagnosis algorithms. The results suggest that (a) for low-shot learning, the MTTNNs trained by minimizing our proposed combined weighted cross-entropy loss perform significantly better than the SOTA low-shot glaucoma diagnosis approach [31] on all four datasets (ACC, Fsc and AUROC are up to 5%, 15% and 0.08 higher, respectively), and (b) for semi-supervised learning, the MTTNNs fine tuned with OVV self-training also achieve the superior performances over another two SOTA semi-supervised glaucoma diagnosis approaches [3, 15] (ACC, Fsc and AUROC are up to 6%, 11% and 0.07 higher, respectively). Compared with the SOTA supervised approaches, the fine tuned MTTNNs demonstrate similar performance on the OHTS test set and better generalizability on three additional test sets. Therefore, we believe that MTTNN with our proposed OVV self-training is an effective SSL technique for low-shot glaucoma diagnosis.

5. Conclusion

The main contributions of this paper include: 1) a *multi-task twin neural network* that can learn glaucoma diagnosis from very limited labeled training data; 2) an effective semi-supervised learning strategy, referred to as *One-Vote Veto self-training*, which can produce pseudo labels of the unlabeled data to fine tune a pretrained multi-task twin neural network. Extensive experiments conducted on four fundus image datasets demonstrated the effectiveness of these proposed techniques. The low-shot learning reduces overfitting and achieves an accuracy on a small training set comparable to a large training set. Furthermore, with One-Vote Veto self-training, the multi-task twin neural networks perform similarly to their backbone CNNs (trained via supervised learning on the full training set) on the OHTS test set and show better generalizability on three additional test sets. With more thresholds and hyper-parameters being tested, we believe our proposed One-Vote Veto self-training strategy can yield better overall performance for semi-supervised glaucoma diagnosis. The methods introduced in this paper can also be applied for other few-shot multi-class biomedical image classification problems, *e.g.*, COVID-19 and lung cancer diagnosis, as discussed in the supplement, and other diseases in which only a small quantity of ground-truth labels are available for network training.

References

- [1] Mohammad Ali Abbas, Syed Usama Khalid Bukhari, Asmara Syed, and Syed Sajid Hussain Shah. The histopathological diagnosis of adenocarcinoma & squamous cells carcinoma of lungs by artificial intelligence: A comparative study of convolutional neural networks. *medRxiv*, 2020. [17](#)
- [2] Jin Mo Ahn, Sangsoo Kim, Kwang-Sung Ahn, Sung-Hoon Cho, Kwan Bok Lee, and Ungsoo Samuel Kim. A deep learning model for the detection of both advanced and early glaucoma using fundus photography. *PloS one*, 13(11):e0207982, 2018. [2](#)
- [3] Manal Al Ghamdi, Mingqi Li, Mohamed Abdel-Mottaleb, and Mohamed Abou Shousha. Semi-supervised transfer learning for convolutional neural networks for glaucoma detection. In *ICASSP*. IEEE, 2019. [2](#), [3](#), [8](#)
- [4] Vijay Badrinarayanan, Alex Kendall, and Roberto Cipolla. Segnet: A deep convolutional encoder-decoder architecture for image segmentation. *IEEE transactions on pattern analysis and machine intelligence*, 39(12):2481–2495, 2017. [12](#)
- [5] Andrew A Borkowski, Marilyn M Bui, L Brannon Thomas, Catherine P Wilson, Lauren A DeLand, and Stephen M Mastorides. Lung and colon cancer histopathological image dataset (lc25000). *CoRR*, 2019. [2](#), [14](#)
- [6] Attila Budai, Rüdiger Bock, Andreas Maier, Joachim Hornegger, and Georg Michelson. Robust vessel segmentation in fundus images. *International journal of biomedical imaging*, 2013, 2013. [12](#)
- [7] Enrique J Carmona, Mariano Rincón, Julián García-Feijóo, and José M Martínez-de-la Casa. Identification of the optic nerve head with genetic algorithms. *Artificial Intelligence in Medicine*, 43(3):243–259, 2008. [13](#)
- [8] Aditya Chattopadhyay, Anirban Sarkar, Prantik Howlader, and Vineeth N Balasubramanian. Grad-cam++: Generalized gradient-based visual explanations for deep convolutional networks. In *2018 IEEE Winter Conference on Applications of Computer Vision (WACV)*, pages 839–847. IEEE, 2018. [14](#), [16](#)
- [9] Liang-Chieh Chen, George Papandreou, Florian Schroff, and Hartwig Adam. Rethinking atrous convolution for semantic image segmentation. *CoRR*, 2017. [5](#), [6](#)
- [10] Liang-Chieh Chen, Yukun Zhu, George Papandreou, Florian Schroff, and Hartwig Adam. Encoder-decoder with atrous separable convolution for semantic image segmentation. In *Proceedings of the European conference on computer vision (ECCV)*, pages 801–818, 2018. [12](#), [13](#)
- [11] Muhammad EH Chowdhury, Tawsifur Rahman, Amith Khandakar, Rashid Mazhar, Muhammad Abdul Kadir, Zaid Bin Mahbub, Khandakar Reajul Islam, Muhammad Salman Khan, Atif Iqbal, Nasser Al Emadi, et al. Can ai help in screening viral and covid-19 pneumonia? *IEEE Access*, 8:132665–132676, 2020. [2](#), [14](#)
- [12] Mark Christopher and et al. Performance of deep learning architectures and transfer learning for detecting glaucomatous optic neuropathy in fundus photographs. *Scientific reports*, 8(1):1–13, 2018. [2](#), [14](#)
- [13] Mark Christopher, Kenichi Nakahara, Christopher Bowd, James A Proudfoot, Akram Belghith, Michael H Goldbaum, Jasmin Rezapour, Robert N Weinreb, Massimo A Fazio, Christopher A Girkin, et al. Effects of study population, labeling and training on glaucoma detection using deep learning algorithms. *TVST*, 9(2):27–27, 2020. [2](#), [6](#)
- [14] J. Deng, W. Dong, R. Socher, L.-J. Li, K. Li, and L. Fei-Fei. ImageNet: A Large-Scale Hierarchical Image Database. In *CVPR*, 2009. [2](#), [6](#)
- [15] Andres Diaz-Pinto, Adrián Colomer, Valery Naranjo, Sandra Morales, Yanwu Xu, and Alejandro F Frangi. Retinal image synthesis and semi-supervised learning for glaucoma assessment. *IEEE TMI*, 38(9):2211–2218, 2019. [2](#), [3](#), [8](#)
- [16] Andrés Díaz Pinto, Sandra Morales Martínez, Valeriana Naranjo Ornedo, Thomas Köhler, José Manuel Mossi García, Amparo Navea Tejerina, et al. Cnns for automatic glaucoma assessment using fundus images: an extensive validation/andres diaz-pinto...[et al.]. *BioMedical Engineering OnLine*, vol. 18 (2019)., 2019. [2](#), [5](#), [6](#), [7](#), [8](#), [12](#), [14](#), [15](#), [16](#)
- [17] Francisco Fumero, Silvia Alayón, José L Sanchez, Jose Sigut, and M Gonzalez-Hernandez. Rim-one: An open retinal image database for optic nerve evaluation. In *2011 24th international symposium on computer-based medical systems (CBMS)*, pages 1–6. IEEE, 2011. [12](#), [13](#)
- [18] Juan J Gómez-Valverde, Alfonso Antón, Gianluca Fatti, Bart Liefers, Alejandra Herranz, Andrés Santos, Clara I Sánchez, and María J Ledesma-Carbayo. Automatic glaucoma classification using color fundus images based on convolutional neural networks and transfer learning. *Biomedical optics express*, 10(2):892–913, 2019. [2](#), [8](#)
- [19] Mae O Gordon, Eve J Higginbotham, Dale K Heuer, Richard K Parrish II, Alan L Robin, Patricia A Morris, Deborah A Dunn, Bradley S Wilson, Michael A Kass, and Ocular Hypertension Treatment Study. Assessment of the impact of an endpoint committee in the ocular hypertension treatment study. *American journal of ophthalmology*, 199:193–199, 2019. [1](#), [2](#), [7](#), [11](#), [12](#), [13](#), [15](#), [16](#)
- [20] Mae O Gordon and Michael A Kass. The ocular hypertension treatment study: design and baseline description of the participants. *Archives of Ophthalmology*, 117(5):573–583, 1999. [1](#), [5](#), [7](#), [11](#)
- [21] Kaiming He, Xiangyu Zhang, Shaoqing Ren, and Jian Sun. Deep residual learning for image recognition. In *CVPR*, pages 770–778, 2016. [2](#), [6](#), [7](#), [13](#), [14](#), [15](#)
- [22] Elad Hoffer and Nir Ailon. Deep metric learning using triplet network. In *International Workshop on Similarity-Based Pattern Recognition*, pages 84–92. Springer, 2015. [4](#)
- [23] Gao Huang, Zhuang Liu, Laurens Van Der Maaten, and Kilian Q Weinberger. Densely connected convolutional networks. In *CVPR*, pages 4700–4708, 2017. [6](#), [7](#), [13](#), [15](#)
- [24] Wenbin Huang, Kai Gao, Yaoming Liu, Mengyin Liang, and Xiulan Zhang. The adverse impact of glaucoma on psychological function and daily physical activity. *Journal of Ophthalmology*, 2020, 2020. [1](#)
- [25] Shruti Jadon. Covid-19 detection from scarce chest x-ray image data using few-shot deep learning approach. In *Medical Imaging 2021: Imaging Informatics for Healthcare, Research, and Applications*, volume 11601, page 116010X. International Society for Optics and Photonics, 2021. [17](#)

- [26] Devesh Jain, Tristan Swedish, Bailey Shen, David Y Kim, Shizuo Mukai, and Ramesh Raskar. Open-source, ultra-low-cost smartphone attachment for non-mydiatic fundus photography-open indirect ophthalmoscope. *IOVS*, 57(12):1685–1685, 2016. [2](#)
- [27] Dr Judy et al. Automated identification of glaucoma from fundus images using deep learning techniques. *European Journal of Molecular & Clinical Medicine*, 7(2):5449–5458, 2020. [2](#), [8](#)
- [28] Michael A Kass, Dale K Heuer, Eve J Higginbotham, Chris A Johnson, John L Keltner, J Philip Miller, Richard K Parrish, M Roy Wilson, and Mae O Gordon. The ocular hypertension treatment study: a randomized trial determines that topical ocular hypotensive medication delays or prevents the onset of primary open-angle glaucoma. *Archives of ophthalmology*, 120(6):701–713, 2002. [1](#), [5](#), [7](#), [8](#), [11](#)
- [29] Alex Kendall, Yarin Gal, and Roberto Cipolla. Multi-task learning using uncertainty to weigh losses for scene geometry and semantics. In *CVPR*, pages 7482–7491, 2018. [4](#)
- [30] Prannay Khosla, Piotr Teterwak, Chen Wang, Aaron Sarna, Yonglong Tian, Phillip Isola, Aaron Maschinot, Ce Liu, and Dilip Krishnan. Supervised contrastive learning. *CoRR*, 2020. [4](#)
- [31] Mijung Kim, Jasper Zuallaert, and Wesley De Neve. Few-shot learning using a small-sized dataset of high-resolution fundus images for glaucoma diagnosis. In *Proceedings of the 2nd International Workshop on Multimedia for Personal Health and Health Care*, pages 89–92, 2017. [2](#), [8](#)
- [32] Gregory Koch, Richard Zemel, and Ruslan Salakhutdinov. Siamese neural networks for one-shot image recognition. In *ICML deep learning workshop*, volume 2. Lille, 2015. [3](#)
- [33] Alex Krizhevsky. One weird trick for parallelizing convolutional neural networks. *CoRR*, 2014. [2](#)
- [34] MiYoung Kwon, Carrie Huisingh, Lindsay A Rhodes, Gerald McGwin Jr, Joanne M Wood, and Cynthia Owsley. Association between glaucoma and at-fault motor vehicle collision involvement among older drivers: a population-based study. *Ophthalmology*, 123(1):109–116, 2016. [1](#)
- [35] Liu Li, Mai Xu, Xiaofei Wang, Lai Jiang, and Hanruo Liu. Attention based glaucoma detection: A large-scale database and cnn model. In *CVPR*, pages 10571–10580, 2019. [1](#), [2](#), [5](#), [6](#), [7](#), [8](#), [11](#), [12](#), [14](#), [15](#), [16](#)
- [36] Zhixi Li, Yifan He, Stuart Keel, Wei Meng, Robert T Chang, and Mingguang He. Efficacy of a deep learning system for detecting glaucomatous optic neuropathy based on color fundus photographs. *Ophthalmology*, 125(8):1199–1206, 2018. [2](#), [8](#)
- [37] Sidong Liu, Stuart L Graham, Angela Schulz, Michael Kalloniatis, Barbara Zangerl, Weidong Cai, Yang Gao, Brian Chua, Hemamalini Arvind, John Grigg, et al. A deep learning-based algorithm identifies glaucomatous discs using monoscopic fundus photographs. *Ophthalmology Glaucoma*, 1(1):15–22, 2018. [2](#)
- [38] Jonathan Long, Evan Shelhamer, and Trevor Darrell. Fully convolutional networks for semantic segmentation. In *Proceedings of the IEEE conference on computer vision and pattern recognition*, pages 3431–3440, 2015. [12](#)
- [39] Laurens van der Maaten and Geoffrey Hinton. Visualizing data using t-sne. *Journal of machine learning research*, 9(Nov):2579–2605, 2008. [6](#), [13](#)
- [40] Everett matthew Lawson and Ramesh Raskar. Smart phone administered fundus imaging without additional imaging optics. *IOVS*, 55(13):1609–1609, 2014. [2](#)
- [41] David McClosky, Eugene Charniak, and Mark Johnson. Effective self-training for parsing. In *Proceedings of the Human Language Technology Conference of the NAACL, Main Conference*, pages 152–159, 2006. [4](#)
- [42] Gerald McGwin Jr, Carrie Huisingh, Shelly Gupta Jain, Christopher A Girkin, and Cynthia Owsley. Binocular visual field impairment in glaucoma and at-fault motor vehicle collisions. *Journal of glaucoma*, 24(2):138, 2015. [1](#)
- [43] Felipe A Medeiros, Alessandro A Jammal, and Eduardo B Mariottoni. Detection of progressive glaucomatous optic nerve damage on fundus photographs with deep learning. *Ophthalmology*, 2020. [2](#), [8](#)
- [44] Alexander Miller, Adam Fisch, Jesse Dodge, Amir-Hossein Karimi, Antoine Bordes, and Jason Weston. Key-value memory networks for directly reading documents. In *Proceedings of the 2016 Conference on Empirical Methods in Natural Language Processing*, pages 1400–1409, 2016. [3](#)
- [45] Pamela Sample et al. The african descent and glaucoma evaluation study (adages): Design and baseline data. *Archives of ophthalmology*, 127(9):1136–1145, 2009. [2](#), [5](#), [6](#), [7](#), [8](#), [14](#), [15](#), [16](#)
- [46] Richard K Parrish, Steven J Gedde, Ingrid U Scott, William J Feuer, Joyce C Schiffman, Carol M Mangione, and Alejandra Montenegro-Piniella. Visual function and quality of life among patients with glaucoma. *Archives of Ophthalmology*, 115(11):1447–1455, 1997. [1](#)
- [47] Alec Radford, Luke Metz, and Soumith Chintala. Unsupervised representation learning with deep convolutional generative adversarial networks. *CoRR*, 2015. [3](#)
- [48] Tawsifur Rahman and et al. Exploring the effect of image enhancement techniques on covid-19 detection using chest x-rays images. *CoRR*, 2020. [2](#), [14](#)
- [49] An Ran Ran and et al. Detection of glaucomatous optic neuropathy with spectral-domain optical coherence tomography: a retrospective training and validation deep-learning analysis. *The Lancet Digital Health*, 1(4):e172–e182, 2019. [2](#)
- [50] Olaf Ronneberger, Philipp Fischer, and Thomas Brox. U-net: Convolutional networks for biomedical image segmentation. In *International Conference on Medical image computing and computer-assisted intervention*, pages 234–241. Springer, 2015. [12](#)
- [51] Mark Sandler, Andrew Howard, Menglong Zhu, Andrey Zhmoginov, and Liang-Chieh Chen. Mobilenetv2: Inverted residuals and linear bottlenecks. In *CVPR*, pages 4510–4520, 2018. [2](#), [6](#), [7](#), [13](#), [14](#), [15](#)
- [52] Ali Serener and Sertan Serte. Transfer learning for early and advanced glaucoma detection with convolutional neural networks. In *2019 Medical Technologies Congress (TIPT-KNO)*, pages 1–4. IEEE, 2019. [2](#), [8](#)
- [53] Karen Simonyan and Andrew Zisserman. Very deep convolutional networks for large-scale image recognition. In *ICLR*, 2015. [2](#)

- [54] Jayanthi Sivaswamy, SR Krishnadas, Gopal Datt Joshi, Madhulika Jain, and A Ujjwaft Syed Tabish. Drishti-gs: Retinal image dataset for optic nerve head (onh) segmentation. In *2014 IEEE 11th international symposium on biomedical imaging (ISBI)*, pages 53–56. IEEE, 2014. 12, 13
- [55] Sainbayar Sukhbaatar, Jason Weston, Rob Fergus, et al. End-to-end memory networks. In *NIPS*, 2015. 4
- [56] Christian Szegedy, Wei Liu, Yangqing Jia, Pierre Sermanet, Scott Reed, Dragomir Anguelov, Dumitru Erhan, Vincent Vanhoucke, and Andrew Rabinovich. Going deeper with convolutions. In *CVPR*, pages 1–9, 2015. 2
- [57] Christian Szegedy, Vincent Vanhoucke, Sergey Ioffe, Jon Shlens, and Zbigniew Wojna. Rethinking the inception architecture for computer vision. In *CVPR*, pages 2818–2826, 2016. 2
- [58] Chuanqi Tan, Fuchun Sun, Tao Kong, Wenchang Zhang, Chao Yang, and Chunfang Liu. A survey on deep transfer learning. In *International conference on artificial neural networks*, pages 270–279. Springer, 2018. 6
- [59] Mingxing Tan and Quoc Le. Efficientnet: Rethinking model scaling for convolutional neural networks. In *ICML*, pages 6105–6114. PMLR, 2019. 6, 7, 13, 15
- [60] Anshul Thakur, Michael Goldbaum, and Siamak Yousefi. Predicting glaucoma before onset using deep learning. *Ophthalmology. Glaucoma*, 3(4):262–268, 2020. 2, 8
- [61] Yih-Chung Tham, Xiang Li, Tien Y Wong, Harry A Quigley, Tin Aung, and Ching-Yu Cheng. Global prevalence of glaucoma and projections of glaucoma burden through 2040: a systematic review and meta-analysis. *Ophthalmology*, 121(11):2081–2090, 2014. 1
- [62] CE Traverso and et al. Direct costs of glaucoma and severity of the disease: a multinational long term study of resource utilisation in europe. *British journal of ophthalmology*, 89(10):1245–1249, 2005. 1
- [63] Isaac Triguero, Salvador Garcíá, and Francisco Herrera. Self-labeled techniques for semi-supervised learning: taxonomy, software and empirical study. *Knowledge and Information systems*, 42(2):245–284, 2015. 3, 4
- [64] Jesper E Van Engelen and Holger H Hoos. A survey on semi-supervised learning. *Machine Learning*, 109(2):373–440, 2020. 3
- [65] Yaqing Wang, Quanming Yao, James T Kwok, and Lionel M Ni. Generalizing from a few examples: A survey on few-shot learning. *ACM Computing Surveys (CSUR)*, 53(3):1–34, 2020. 2
- [66] Robert N Weinreb and Peng Tee Khaw. Primary open-angle glaucoma. *The Lancet*, 363(9422):1711–1720, 2004. 1
- [67] Peng Zhou, Wei Shi, Jun Tian, Zhenyu Qi, Bingchen Li, Hongwei Hao, and Bo Xu. Attention-based bidirectional long short-term memory networks for relation classification. In *Proceedings of the 54th annual meeting of the association for computational linguistics (volume 2: Short papers)*, pages 207–212, 2016. 3

6. Supplementary Material

6.1. Ocular Hypertension Treatment Study

The Ocular Hypertension Treatment Study (OHTS) [20, 28] was initiated in 1994 and it is the first large randomized clinical trial to document the safety and efficacy of topical ocular hypertensive medication in preventing/delaying the onset of visual field and/or optic nerve damage in subjects with ocular hypertension at moderate risk for developing primary open-angle glaucoma. **The recruited 1636 participants did not have glaucoma at study entry.** Each participant was seen twice a year for Humphrey 30-2 visual field testing and once a year for stereoscopic optic nerve head photographs. Compared with other commonly used fundus image datasets detailed in Tab. 5, the OHTS [19] dataset is

- much larger (~ 15 times larger than the recently published *large-scale attention based glaucoma (LAG) dataset*² [35]);
- more diverse – the enrolled participants of **more than six different races**: (1) native American or Alaskan native, (2) Asian, (3) African American, (4) Hispanic, (5) white, and (6) other, were examined at **22 institutes** (John Hopkins University, UCLA, UCSD, etc.) using different instruments for **over 15 years**.

Such a large-scale, imbalanced, longitudinal fundus image dataset provides us a basis to explore the feasibility of:

- learning glaucoma diagnosis on an extremely imbalanced dataset of fundus images acquired from participants of different races using different instruments at different institutes;
- low-shot glaucoma diagnosis when only a small amount of labeled data is available;
- semi-supervised glaucoma diagnosis when raw data is abundant, but labeling resources are scarce, costly, require strong expertise, or are just unavailable.

6.2. Performance Evaluation Metrics

This section provides details on the metrics used in this paper. TP, TN, FP, and FN denote the numbers of true positive, true negative, false positive, and false negative classifications, respectively.

- Accuracy (ACC) refers to the proportion of correct classifications:

$$\text{ACC} = \frac{\text{TP} + \text{TN}}{\text{TP} + \text{TN} + \text{FP} + \text{FN}}. \quad (6)$$

ACC can be a misleading metric when the dataset is imbalanced.

²The number of fundus images being published is fewer than what was reported in publication [35]

Dataset	Number of fundus images			Country	Publication year	Number of institute(s) for data collection	Number of race(s)
	Healthy	GON	Total				
ACRIMA [16]	309	396	705	Spain	2019	1	1
LAG [35]	3143	1711	4854	China	2019	1	1
RIM-ONE [17]	255	200	455	Spain	2011	3	1
DRISHTI-GS [54]	31	70	101	India	2014	1	1
HRF [6]	15	15	30	Germany	2013	1	1
OHTS [19]	71176	3502	74678	U.S.A.	2019	22	≥ 6

Table 5: Comparisons between the OHTS [19] dataset and other commonly used fundus images datasets, where GON refers to glaucomatous optic neuropathy.

- Precision (PRE) measures the proportion of positive classifications that are actually correct:

$$PRE = \frac{TP}{TP + FP}. \quad (7)$$

- Sensitivity (SEN), also known as recall (REC) or true positive rate (TPR), measures the proportion of positive pixels or images that are correctly classified:

$$SEN = REC = \frac{TP}{TP + FN}. \quad (8)$$

- Specificity (SPE), also known as true negative rate (TNR), measures the proportion of negative pixels or images that are correctly classified:

$$SPE = \frac{TN}{TN + FP}. \quad (9)$$

- F-score (Fsc) is the harmonic mean of PRE and REC:

$$Fsc = 2 \frac{PRE \times REC}{PRE + REC}. \quad (10)$$

It is widely utilized in image classification and semantic segmentation tasks, especially when the classes are imbalanced.

- Matthews correlation coefficient (MCC) is a widely used metric to measure the binary classification quality even if the dataset is imbalanced:

$$MCC =$$

$$\frac{TP \times TN - FP \times FN}{\sqrt{(TP + FP)(TP + FN)(TN + FP)(TN + FN)}}. \quad (11)$$

MCC is utilized as an additional metric in the supplement to select the best λ for low-shot learning.

- Intersection over union (IoU)

$$IoU = \frac{TP}{FN + FP} \quad (12)$$

is utilized in the supplement to evaluate the performance of semantic segmentation CNNs for optic nerve head extraction.

- AUROC refers to the area underneath the receiver operating characteristic (ROC) curve, whose horizontal and vertical axes are false positive rate (FPR) and TPR, respectively, where $FPR = 1 - TNR$.

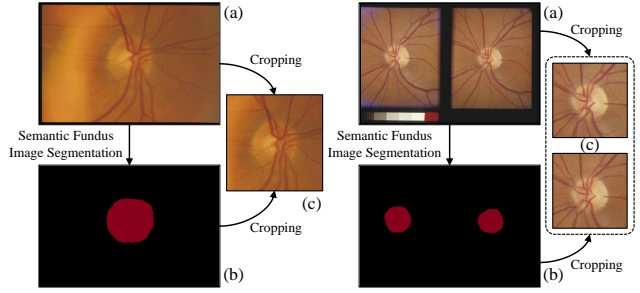


Figure 3: Examples of semantic fundus image segmentation for optic nerve head extraction: (a) raw fundus photographs; (b) semantic segmentation results, where the optic nerve head areas are shown in red; (c) cropped fundus images used for CNN training.

Network	PRE (%)	REC (%)	ACC (%)	Fsc (%)	IoU (%)
U-Net [50]	70.08	67.87	97.93	68.96	52.62
SegNet [4]	79.06	92.68	98.92	85.33	74.41
FCN [38]	88.00	96.79	99.44	92.19	85.51
DeepLabv3+ [10]	96.68	95.93	99.75	96.30	92.87

Table 6: Comparisons of U-Net [50], FCN [38], SegNet [4], and DeepLabv3+ [10] for optic nerve head extraction. The best results are shown in bold type.

6.3. Dataset Preparation

As mentioned above, the fundus image datasets utilized in our experiments were collected at various intervals by different clinicians from different institutes using different fundus cameras. Since they were collected for clinical research purposes and not for evaluating computer vision algorithms, this leads to significant variability in image quality and resolution and can make the CNN training much more challenging than expected. To this end, prior to training CNNs for glaucoma diagnosis, we first cropped a region centered on the optic nerve head from each raw fundus photograph using a semantic segmentation CNN trained for optic nerve head extraction.

In our experiments, we trained four semantic segmentation CNNs: 1) U-Net [50], fully convolutional network (FCN) [38], 3) SegNet [4], and 4) DeepLabv3+ [10], on three public optic nerve head segmentation datasets: 1)

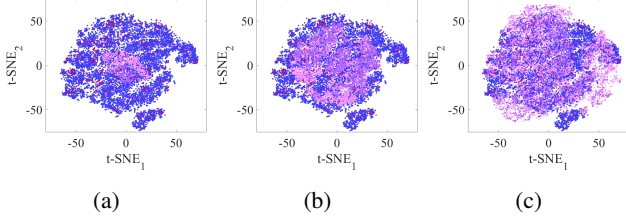


Figure 4: Comparisons of dataset visualizations produced by t-SNE [39], where \bullet and \bullet represent the healthy and GON images in the OHTS test set, respectively; \bullet and \bullet in (a) represent the healthy and GON images in the ACRIMA dataset, respectively; \bullet and \bullet in (b) represent the healthy and GON images in the LAG dataset, respectively; \bullet and \bullet in (c) represent the healthy and GON images in the DIGS/ADAGES dataset, respectively.

DRIONS-DB [7], 2) DRISHTI-GS [54], and 3) RIM-ONE [17], in which the pixel-level optic nerve head ground-truth labels are available. The quantitative comparisons are shown in Tab. 6. It can be seen that DeepLabv3+ [10] achieves the best PRE, ACC, Fsc, and IoU. We then randomly selected 200 fundus images from the OHTS [19] dataset and manually labeled their optic nerve head ground truth to fine tune our pretrained DeepLabv3+ [10]. It was subsequently applied to the entire OHTS, LAG, and DIGS/ADAGES datasets to extract regions centered on the optic nerve heads from raw fundus photographs. The ACRIMA dataset is already aligned. Examples of the extracted regions are shown in Fig. 3. Our well-trained DeepLabv3+ [10] model will also be publicly available upon publication.

6.4. Dataset Visualization Using t-SNE

Visualizations of the four test sets using t-SNE [39] are shown in Fig. 4. It can be observed that the healthy and GON images are distributed similarly between the OHTS and LAG datasets, but the ACRIMA and DIGS/ADAGES datasets have dissimilar distributions to the OHTS test set. Hence, we expect models trained on the OHTS dataset to perform similarly on the LAG dataset, but somewhat worse on the ACRIMA and DIGS/ADAGES datasets.

6.5. Supplementary Ablation Study on Low-Shot Learning

In our experiments, we respectively set λ used in our proposed combined weighted cross-entropy loss to 0.1, 0.2, 0.3, 0.4, and 0.5 and compare the MTTNN performance when $\Phi(\cdot)$ performs vector absolute difference (VAD) and vector squared difference (VSD). The comparisons in terms of Fsc, MCC, and AUROC on the OHTS test set are provided in Fig. 5. It can be obviously seen that when $\lambda = 0.3$, the MTTNN achieves the best overall performance, which

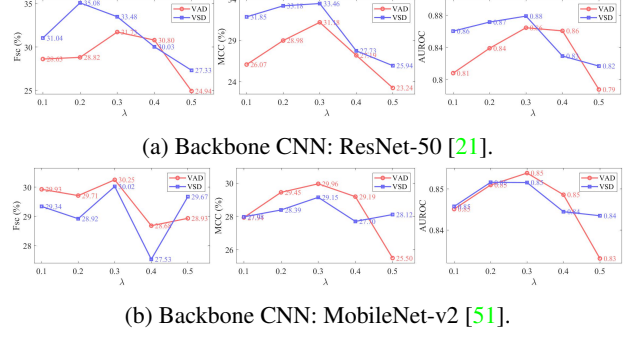


Figure 5: MTTNN performance w.r.t. different λ and $\Phi(\cdot)$.

is reasonable, as a higher λ weighs more on the image classification task, easily resulting in overfitting. In addition, VSD outperforms VAD when using ResNet-50 [21] as the MTTNN backbone CNN, while VAD outperforms VSD when using MobileNet-v2 [51] as the MTTNN backbone CNN. To validate the generalizability of the well-trained MTTNNs, we further evaluate them on three additional datasets, as shown in Tab. 7. Compared with VSD, when $\Phi(\cdot)$ applies VAD, the MTTNN generally performs better or very similarly on the additional test sets, especially when testing the MTTNN assembled with ResNet-50 [21] on the ACRIMA dataset. VAD is therefore used in the following experiments. Furthermore, Tab. 7 shows a baseline supervised learning experiment conducted on the low-shot training set (containing 1147 fundus images). The results suggest that low-shot learning performs much better than supervised learning when the training size is small.

6.6. Supplementary Comparisons of Supervised Learning, Low-Shot Learning and Semi-Supervised Learning

Tab. 1 in the full paper is a subset of Tab. 8 in the supplement, which provides the supplementary comparisons of supervised learning, low-shot learning, and semi-supervised learning. These results suggest that our low-shot learning with *multi-task twin neural network* and semi-supervised learning with *One-Vote Veto (OVV) self-training* that require only a small amount of labeled training data, perform similarly and, in some cases, better than the backbone CNNs trained through supervised learning on the entire OHTS training set. Specifically, MTTNN assembled with ResNet-50 [21] performs significantly better than the conventional ResNet-50 [21] on all three additional test sets. When using MobileNet-v2 [51] or DenseNet [23], the MTTNN performs similarly, and in some cases, better than the backbone CNN trained through supervised learning. Moreover, EfficientNet [59] trained through supervised learning performs unsatisfactorily on all four test sets, but it is considerably compatible with MTTNN for low-shot and semi-supervised

Test set	Experiments	Training strategy	ResNet-50 [21]				MobileNet-v2 [51]			
			ACC (%)	Fsc (%)	MCC (%)	AUROC	ACC (%)	Fsc (%)	MCC (%)	AUROC
ACRIMA [16]	Baseline	Supervised learning	57.163	56.734	16.387	0.625	73.333	78.341	45.505	0.779
	VAD	Low-shot learning	67.092	63.175	41.015	0.758	70.355	67.797	46.421	0.820
	VSD	Low-shot learning	49.504	25.523	13.322	0.437	66.241	59.107	43.800	0.823
LAG [35]	Baseline	Supervised learning	64.318	57.445	29.116	0.714	65.122	63.268	38.373	0.781
	VAD	Low-shot learning	79.028	65.908	52.381	0.841	79.007	69.482	53.536	0.843
	VSD	Low-shot learning	78.039	68.179	51.452	0.826	78.430	61.830	51.035	0.846
DIGS/ADAGES [45]	Baseline	Supervised learning	59.639	59.708	19.674	0.648	61.478	66.128	26.319	0.669
	VAD	Low-shot learning	67.745	60.754	35.505	0.743	69.176	68.145	38.363	0.748
	VSD	Low-shot learning	65.736	55.722	31.918	0.700	68.120	64.028	35.869	0.740

Table 7: Supervised learning on a small amount of training data vs. low-shot learning. λ is set to 0.3. The best results are shown in bold font.

glaucoma diagnosis.

6.7. Class Activation Map Visualization

We also employ Grad-CAM++ [8] to explain the models compared in Tab. 8, as shown in Fig. 6. These results suggest that the optic nerve head areas have the greatest impact on model decisions. The neuroretinal rim areas are identified as most important, and the periphery contributed comparatively little to model decisions for both healthy and GON eyes [12].

6.8. MTTNN and Combined Weighted Cross-Entropy Loss for Few-Shot Biomedical Image Classification

Moreover, we conduct two additional few-shot lung disease diagnosis experiments: (a) chest x-ray image classification for COVID-19 and viral pneumonia detection [11, 48], and (b) lung histopathological image classification for lung cancer diagnosis [5], to validate the effectiveness of our proposed MTTNN and combined weighted cross-entropy loss. The first experiment has three classes of images: (1) healthy, (2) viral pneumonia, and (3) COVID-19 (an example of each class is shown in Fig. 7), while the second experiment also has three classes of images to detect lung cancer as: (1) benign tissue, (2) adenocarcinoma, and (3) squamous cell carcinoma (an example of each class is shown in Fig. 7). In these two experiments, we only select few images from each class for MTTNN training. The numbers of images used for training, validation, and testing are given in Tab. 9, where it can be observed that the training set is much smaller than the validation and test sets. Since the combined weighted cross-entropy loss introduced in the full paper can only be used for binary image classification problems, we extend it here to tackle multi-class image classification problems.

Let us take the aforementioned chest x-ray image classification task as an example. Each image \mathbf{x} is assigned a pair of two labels (r, s) . Their values are:

- $r = 1$ and $s = 0$, when \mathbf{x} is a healthy image;

- $r = 2$ and $s = 1$, when \mathbf{x} is a viral pneumonia image;
- $r = 3$ and $s = 3$, when \mathbf{x} is a COVID-19 image.

We denote the numbers of healthy images (class 1), viral pneumonia images (class 2), and COVID-19 images (class 3) as n_1, n_2 , and n_3 , respectively. The total number of images is $N = n_1 + n_2 + n_3$. The weight $\omega_{\text{cla},e}$ used in the image classification loss \mathcal{L}_{cla} w.r.t. class e is:

$$\omega_{\text{cla},e} = \frac{N - n_e}{2N}. \quad (13)$$

$\sum_{e=1}^3 \omega_{\text{cla},e} = 1$. Therefore, \mathcal{L}_{cla} can be written as follows:

$$\mathcal{L}_{\text{cla}}(\mathbf{z}) = - \sum_{e=1}^3 \omega_{\text{cla},e} \left(k_{e,i} \log(p_e(\mathbf{x}_i)) + k_{e,j} \log(p_e(\mathbf{x}_j)) \right), \quad (14)$$

where $p_e(\mathbf{x}) \in [0, 1]$ indicates the probability that \mathbf{x} belongs to class e . $\sum_{e=1}^3 p_e(\mathbf{x}) = 1$. $k_{e,i} = 1$ when $e = r_i$, and $k_{e,i} = 0$ otherwise. Given a pair of images \mathbf{x}_i and \mathbf{x}_j , whose ground-truth labels are (r_i, s_i) and (r_j, s_j) , respectively, there are four cases:

- case 1: $|s_i - s_j| = 1$ (healthy vs. viral pneumonia);
- case 2: $|s_i - s_j| = 2$ (viral pneumonia vs. COVID-19);
- case 3: $|s_i - s_j| = 3$ (COVID-19 vs. healthy);
- case 4: $|s_i - s_j| = 0$ (two images are of the same class).

The weight $\omega_{\text{sim},c}$ used in the image similarity comparison loss \mathcal{L}_{sim} w.r.t. case c is:

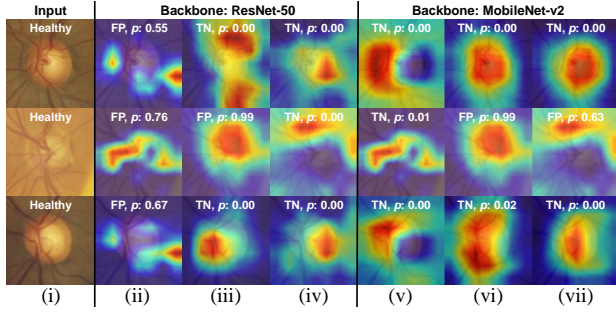
$$\omega_{\text{sim},c} = \begin{cases} 1 - \frac{2n_1n_2}{N(N-1)} & \text{if } c = 1 \\ 1 - \frac{2n_2n_3}{N(N-1)} & \text{if } c = 2 \\ 1 - \frac{2n_1n_3}{N(N-1)} & \text{if } c = 3 \\ 1 - \frac{\sum_{w=1}^3 n_w(n_w-1)}{N(N-1)} & \text{if } c = 4 \end{cases}, \quad (15)$$

$\sum_{c=1}^4 \omega_{\text{sim},c} = 1$. Therefore, \mathcal{L}_{sim} can be written as follows:

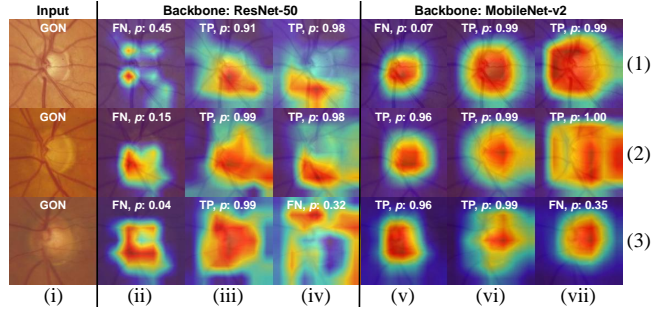
$$\mathcal{L}_{\text{sim}}(\mathbf{z}) = - \sum_{c=1}^4 \omega_{\text{sim},c} h_{c,(i,j)} \log(q_c(\mathbf{x}_i, \mathbf{x}_j)), \quad (16)$$

Backbone CNN	Experiment		OHTS [19]		ACRIMA [16]		LAG [35]		DIGS/ADAGES [45]	
			90% SPE	95% SPE	90% SPE	95% SPE	90% SPE	95% SPE	90% SPE	95% SPE
ResNet-50 [21]	Baseline	AUROC (95% CI)	0.904 (0.865, 0.935)		0.736 (0.698, 0.771)		0.794 (0.780, 0.807)		0.744 (0.696, 0.792)	
		SEN	0.71	0.54	0.38	0.29	0.53	0.42	0.43	0.30
		ACC	0.89	0.93	0.61	0.58	0.77	0.76	0.68	0.64
		FP	1167	584	31	15	314	157	155	78
		FN	175	279	244	280	811	999	792	972
		TP	430	326	152	116	900	712	594	414
		TN	10506	11089	278	294	2829	2986	1395	1472
	MTTNN	AUROC (95% CI)	0.869 (0.833, 0.901)		0.758 (0.723, 0.792)		0.841 (0.829, 0.853)		0.743 (0.683, 0.795)	
		SEN	0.58	0.38	0.45	0.31	0.59	0.45	0.37	0.23
		ACC	0.88	0.92	0.65	0.59	0.79	0.78	0.65	0.61
		FP	1167	584	31	15	314	157	155	78
		FN	253	378	216	272	709	934	868	1073
		TP	352	227	180	124	1002	777	518	313
		TN	10506	11089	278	294	2829	2986	1395	1472
	MTTNN+OVV	AUROC (95% CI)	0.898 (0.857, 0.928)		0.775 (0.741, 0.808)		0.881 (0.870, 0.891)		0.763 (0.695, 0.820)	
		SEN	0.71	0.55	0.37	0.29	0.69	0.57	0.40	0.23
		ACC	0.89	0.93	0.60	0.58	0.83	0.81	0.66	0.61
		FP	1167	584	31	15	314	157	155	78
		FN	177	275	250	281	528	742	835	1062
		TP	428	330	146	115	1183	969	551	324
		TN	10506	11089	278	294	2829	2986	1395	1472
MobileNet-v2 [51]	Baseline	AUROC (95% CI)	0.893 (0.845, 0.932)		0.794 (0.760, 0.825)		0.856 (0.844, 0.867)		0.786 (0.728, 0.835)	
		SEN	0.69	0.56	0.52	0.39	0.63	0.53	0.51	0.32
		ACC	0.89	0.93	0.69	0.63	0.80	0.80	0.71	0.65
		FP	1167	584	31	15	314	157	155	78
		FN	186	265	190	243	636	804	686	937
		TP	419	340	206	153	1075	907	700	449
		TN	10506	11089	278	294	2829	2986	1395	1472
	MTTNN	AUROC (95% CI)	0.859 (0.813, 0.896)		0.820 (0.786, 0.850)		0.843 (0.831, 0.855)		0.748 (0.689, 0.802)	
		SEN	0.57	0.38	0.54	0.37	0.58	0.43	0.32	0.17
		ACC	0.88	0.92	0.70	0.62	0.79	0.77	0.63	0.58
		FP	1167	584	31	15	314	157	155	78
		FN	258	373	183	249	715	967	942	1156
		TP	347	232	213	147	996	744	444	230
		TN	10506	11089	278	294	2829	2986	1395	1472
	MTTNN+OVV	AUROC (95% CI)	0.887 (0.850, 0.920)		0.840 (0.808, 0.867)		0.851 (0.838, 0.862)		0.777 (0.718, 0.826)	
		SEN	0.64	0.46	0.60	0.46	0.63	0.49	0.39	0.19
		ACC	0.89	0.93	0.73	0.68	0.80	0.79	0.66	0.59
		FP	1167	584	31	15	314	157	155	78
		FN	217	328	160	213	641	875	842	1117
		TP	388	277	236	183	1070	836	544	269
		TN	10506	11089	278	294	2829	2986	1395	1472
DenseNet [23]	Baseline	AUROC (95% CI)	0.898 (0.867, 0.927)		0.810 (0.778, 0.841)		0.784 (0.771, 0.798)		0.743 (0.688, 0.789)	
		SEN	0.71	0.55	0.50	0.29	0.47	0.34	0.34	0.22
		ACC	0.89	0.93	0.68	0.58	0.75	0.74	0.64	0.60
		FP	1228	614	31	15	314	157	155	78
		FN	181	277	197	280	915	1121	912	1086
		TP	437	341	199	116	796	590	474	300
		TN	11049	11663	278	294	2829	2986	1395	1472
	MTTNN	AUROC (95% CI)	0.854 (0.811, 0.894)		0.753 (0.716, 0.786)		0.853 (0.842, 0.865)		0.732 (0.675, 0.785)	
		SEN	0.58	0.39	0.50	0.40	0.60	0.50	0.36	0.23
		ACC	0.88	0.92	0.68	0.64	0.80	0.79	0.64	0.61
		FP	1228	614	31	15	314	157	155	78
		FN	262	378	197	237	680	850	892	1072
		TP	356	240	199	159	1031	861	494	314
		TN	11049	11663	278	294	2829	2986	1395	1472
	MTTNN+OVV	AUROC (95% CI)	0.896 (0.861, 0.926)		0.783 (0.748, 0.817)		0.831 (0.818, 0.843)		0.746 (0.678, 0.800)	
		SEN	0.67	0.52	0.49	0.28	0.60	0.44	0.40	0.23
		ACC	0.89	0.93	0.67	0.57	0.79	0.77	0.66	0.61
		FP	1228	614	31	15	314	157	155	78
		FN	203	294	200	285	685	958	830	1063
		TP	415	324	196	111	1026	753	556	323
		TN	11049	11663	278	294	2829	2986	1395	1472
EfficientNet [59]	Baseline	AUROC (95% CI)	0.768 (0.684, 0.834)		0.633 (0.590, 0.672)		0.650 (0.634, 0.667)		0.658 (0.611, 0.702)	
		SEN	0.41	0.27	0.18	0.09	0.23	0.13	0.27	0.14
		ACC	0.88	0.92	0.50	0.47	0.67	0.66	0.60	0.57
		FP	1228	614	31	15	314	157	155	78
		FN	362	452	323	360	1311	1493	1014	1189
		TP	256	166	73	36	400	218	372	197
		TN	11049	11663	278	294	2829	2986	1395	1472
	MTTNN	AUROC (95% CI)	0.863 (0.818, 0.899)		0.845 (0.815, 0.873)		0.845 (0.833, 0.856)		0.719 (0.659, 0.774)	
		SEN	0.56	0.37	0.48	0.33	0.56	0.42	0.29	0.15
		ACC	0.88	0.92	0.67	0.60	0.78	0.76	0.61	0.57
		FP	1228	614	31	15	314	157	155	78
		FN	272	391	204	267	754	989	988	1185
		TP	346	227	192	129	957	722	398	201
		TN	11049	11663	278	294	2829	2986	1395	1472
	MTTNN+OVV	AUROC (95% CI)	0.886 (0.845, 0.918)		0.792 (0.758, 0.824)		0.850 (0.837, 0.861)		0.749 (0.690, 0.800)	
		SEN	0.62	0.48	0.44	0.30	0.63	0.47	0.35	0.22
		ACC	0.89	0.93	0.64	0.58	0.81	0.78	0.64	0.60
		FP	1228	614	31	15	314	157	155	78
		FN	235	324	220	278	630	909	901	1085
		TP	383	294	176	118	1081	802	485	301
		TN	11049	11663	278	294	2829	2986	1395	1472

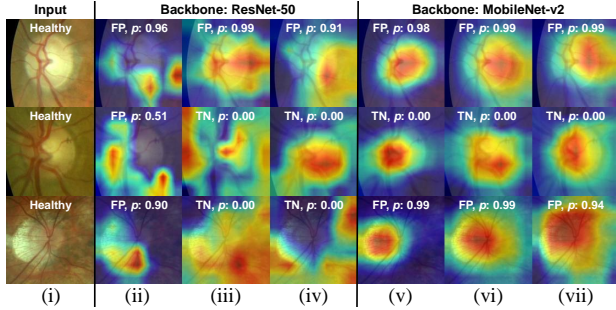
Table 8: AUROC (shown along with 95% CI), sensitivity, accuracy, FP, FN, TP, and TN w.r.t. 90% specificity and 95% specificity of supervised learning, low-shot learning, and semi-supervised learning.



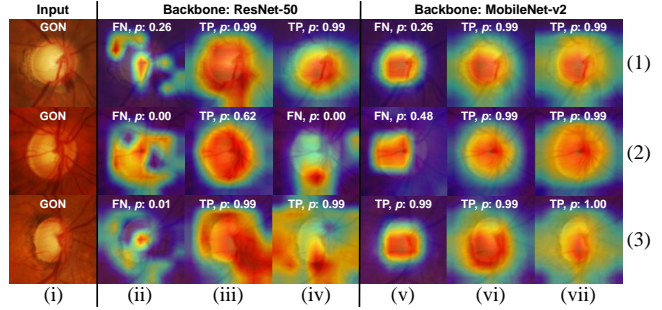
(a) OHTS [19] healthy fundus images.



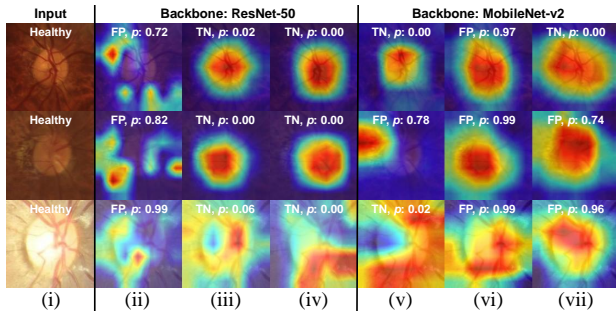
(b) OHTS [19] GON fundus images.



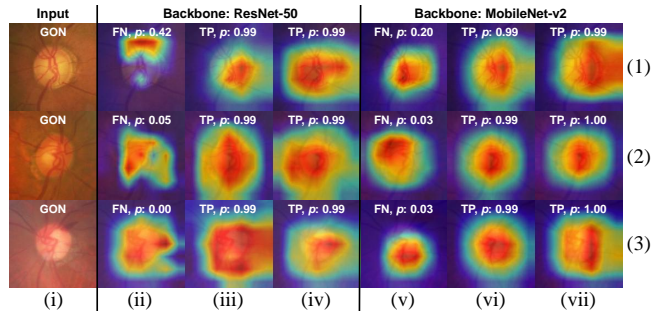
(c) ACRIMA [16] healthy fundus images.



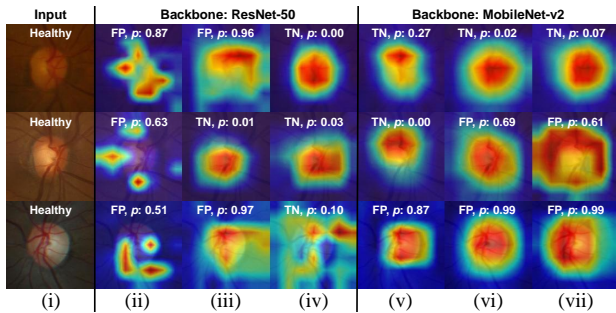
(d) ACRIMA [16] GON fundus images.



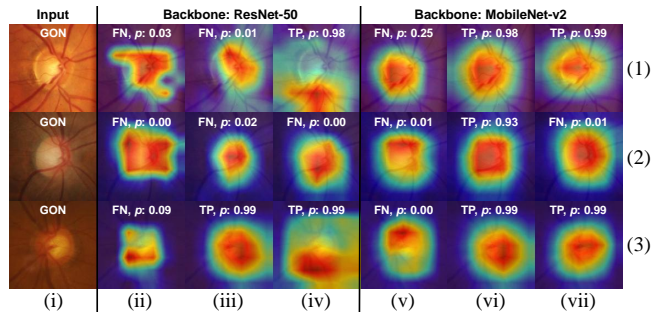
(e) LAG [35] healthy fundus images.



(f) LAG [35] GON fundus images.



(g) DIGs/ADAGES [45] healthy fundus images.



(h) DIGs/ADAGES [45] GON fundus images.

Figure 6: Examples of Grad-CAM++ [8] results: (i) fundus images; (ii) and (v) show the class activation maps of (i), obtained by the backbone CNNs trained through supervised learning on the entire training set (containing $\sim 53K$ fundus images); (iii) and (vi) show the class activation maps of (i), obtained by MTTNNs trained through low-shot learning on a small training set (containing 1147 fundus images); (iv) and (vii) show the class activation maps of (i), obtained by MTTNNs fine tuned with our proposed OVV self-training on the entire training set (containing $\sim 53K$ fundus images without ground-truth labels).

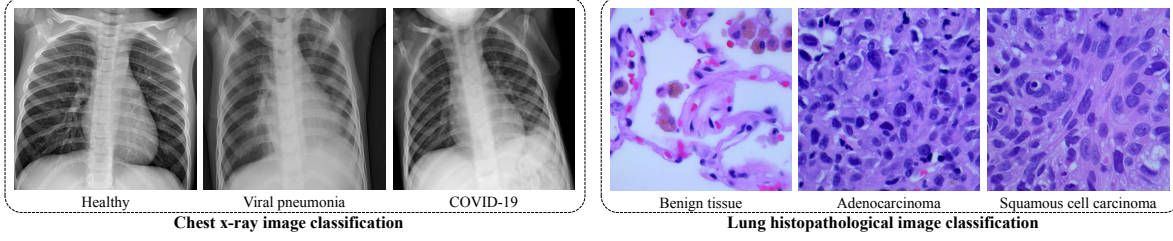


Figure 7: Examples of images used in two few-shot lung disease diagnosis tasks.

		PRE			
Prediction	Healthy	622 32.7%	44 2.3%	9 0.5%	92.1% 7.9%
	Viral pneumonia	31 1.6%	605 31.8%	27 1.4%	91.3% 8.7%
	COVID-19	4 0.2%	10 0.5%	552 29.0%	97.5% 2.5%
	REC	94.7% 5.3%	91.8% 8.2%	93.9% 6.1%	93.4% 6.6%
		ACC			
		Healthy	Viral pneumonia	COVID-19	
		Ground truth			
		Chest x-ray image classification			

		PRE			
Prediction	Benign tissue	2462 32.9%	142 1.9%	8 0.1%	94.3% 5.7%
	Adenocarcinoma	33 0.4%	2149 28.7%	388 5.2%	83.6% 16.4%
	Squamous cell carcinoma	0 0.0%	204 2.7%	2099 28.0%	91.1% 8.9%
	REC	98.7% 1.3%	86.1% 13.9%	84.1% 15.9%	89.6% 10.4%
		ACC			
		Benign tissue	Adenocarcinoma	Squamous cell carcinoma	
		Ground truth			
		Lung histopathological image classification			

Figure 8: MTTNN results for two few-shot lung disease diagnosis tasks.

Class	Training	Validation	Test
Healthy	27	657	657
Viral pneumonia	27	659	659
COVID-19	24	588	588

(a) Chest x-ray image classification.

Class	Training	Validation	Test
Benign tissue	10	2495	2495
Adenocarcinoma	10	2495	2495
Squamous cell carcinoma	10	2495	2495

(b) Lung histopathological image classification.

Table 9: Training, validation, and test sample sizes in the two few-shot biomedical image classification experiments.

where $q_c(\mathbf{x}_i, \mathbf{x}_j) \in [0, 1]$ indicates the similarity between \mathbf{x}_i and \mathbf{x}_j under case c . $\sum_{c=1}^4 q_c(\mathbf{x}_i, \mathbf{x}_j) = 1$. $h_{c,(i,j)} = 1$ when \mathbf{x}_i and \mathbf{x}_j belong to case c , and $h_{c,(i,j)} = 0$ otherwise. The hyper-parameter λ is set to 0.3, as discussed above.

The experimental results of these two multi-task biomedical image classification tasks are shown with two confusion matrices in Fig. 8. These results suggest that our proposed MTTNN can also be trained with very few images to solve multi-class biomedical image classification problems. The achieved accuracy for chest x-ray image classification (~ 25 -shot learning) and lung histopathological image classification (10-shot learning) are 93% and 90%, respectively. Specifically, the chest x-ray image classification result compares favorably to the accuracy of 82%-93% achieved by

supervised methods (2520 images for training, 840 images for validation, and 840 images for testing) using all available training data [25]. Although the accuracy achieved by MTTNN for lung histopathological image classification is lower than that (over 97% reported in [1]) achieved by supervised approaches using the full training set (8250 images for training, 10494 images for validation, and 3744 images for testing), we believe our proposed low-shot learning method can achieve comparable results when a small amount of additional images are incorporated for MTTNN training.